nature nanotechnology

Article

https://doi.org/10.1038/s41565-023-01453-9

Close the cancer–immunity cycle by integrating lipid nanoparticle–mRNA formulations and dendritic cell therapy

In the format provided by the authors and unedited

Table-of-contents

Supplementary Discussion

The immunosuppressive TME hampers the stepwise immune activation in the CIC, leading to uncontrollable tumor growth, metastasis, and relapse[1-10]. Dendritic cells, as intermediators in the CIC, are an important determinant for the development of antitumor immunity[1-5]. Due to the limited therapeutic effects of adoptive DC transfer, many clinical strategies have focused on combining DC therapy with other therapeutics, such as chemotherapeutic drugs and antibodies[3,4,11-14]. In this study, we developed an alternative combination treatment regimen termed CATCH, which utilized two types of LNP-mRNA formulations to boost DC therapy via integrating ICD effects in tumoral tissues and CD40-CD40L activation in DCs. We first synthesized a library of sugar alcohol-derived ionizable lipids and explored the structure-activity relationship of the formulated LNPs. We found that multiple parameters of chemical structures can dramatically influence particle formulations and their bioactivity. By quantifying the luminescence intensity in BMDCs (Fig. 2a), we found that chirality of the amine cores could affect mRNA delivery efficacy of the formulated LNPs. The amine cores of DIS and LIS lipids were a pair of enantiomers and they showed similar mRNA delivery capacity, especially DIS-1 to 8 and LIS-1 to 8. Lipids with C10 hydrocarbon tails resulted in more effective mRNA delivery than lipids containing other hydrocarbon tails. On the other hand, the DIM series displayed a different trend. Among the DIM series, DIM-7 was the most effective in mRNA delivery. The length of hydrocarbon (LIS2-6, DIS2-6, and DIM2-6) could be tuned to improve mRNA delivery efficacy. Lipids containing carbonate ester linkers (DIS8, DIM8, and LIS8) in the hydrophobic domains showed weak mRNA delivery ability. Through in vitro studies, we identified two optimal LNP formulations, DIM7S and LIS10W, for effective mRNA delivery. DIM7S showed higher mRNA delivery efficacy in BMDCs than the state-of-art delivery technologies (Supplementary Fig. 1f). LIS10W induced robust ICD in melanoma tissues (Fig. 3f) and effectively delivered mRNA into melanoma cells (Supplementary Fig. 4a).

To evaluate the therapeutic potential of CATCH (CD40L-LIS10W+CD40-BDMCs) treatment regimen, we first i.t. administrated CD40L-LIS10W to simultaneously induce ICD and CD40L expression in tumoral tissues. Next, we i.t. adoptively transferred CD40-BMDCs that were ex vivo engineered by CD40-DIM7S. We observed that both CD40L-LIS10W and CD40-BDMCs induced multiple cytokines and chemokines in tumoral tissues and blood (Fig. 4k, l). However, the concentrations induced by CD40L-LIS10W alone gradually decreased post administration until the injection of CD40-BDMCs. Thus, CATCH treatment (CD40L-LIS10W+CD40-BDMCs) could better reprogram the immunosuppressive TME and boost systemic immunity than CD40L-LIS10W alone. For example, CATCH treatment induced higher levels of IL-12 than CD40L-LIS10W treatment, which can facilitate the differentiation of naive T cells into type 1 T helper cells and stimulate the cytotoxic activities of $CD8^+$ T cells[15]. Additionally, the upregulation of multiple chemokines, such as CCL5, and CXCL9, facilitated the recruitment of DCs and T cells to tumoral lesions[16,17]. In accordance with these changes, mRNAs involving in T cell trafficking and migration, including *Spn* and *Gpr183*, were increased[18,19]. Notably, the reprogrammed TME elevated the levels of antitumor phenotype of endogenous APCs with upregulated costimulatory molecules and MHC transcripts (Fig. 5d, e, Supplementary Fig.8d), indicating an enhanced TAA presentation ability[20,21]. Given the upregulated T cell receptor-associated transcripts, such as *Cd247* and *Lck* (Fig. 5d, e), this treatment regimen may contribute to the interaction between endogenous APCs and T cells, promoting the development of tumor-specific T cells[22]. Prior studies reported that the adoptively transferred DCs may transfer TAAs to endogenous DCs for the generation of

T cell immunity[23]. Our results also revealed that CATCH treatment enhanced T cell priming ability of endogenous DCs (Supplementary Fig. 9d, e). Moreover, the depletion of endogenous DCs compromised the survival of this treatment regimen (Fig. 4i). All these data suggest the important antitumor effects of both endogenous and adoptively transferred DCs in CATCH treatment. As a result, T cells were primed to increase the production of IFN-γ, TNF-α, and granzymes (Supplementary Fig. 8e). Likewise, $CD8^+$ T cell cytotoxicity-related mRNAs (e.g., *Gzma, Gzmb*, and *Prf1*) and T cell costimulatory molecule-related mRNAs (e.g., *Icos* and *Cd2*) were upregulated (Fig. 5d, e). The survival and expansion of tumor-infiltrating $CD8^+$ T cells are essential for tumor elimination[24,25]. Nevertheless, the immunosuppressive TME limits $CD8^+$ T cell activation and contributes to their exhaustion[24,25]. This state is characterized by weakened cytotoxic functions and increased inhibitory receptors, ultimately resulting in cancer immune evasion[24,25]. The CATCH treatment may ameliorate T cell exhaustion via reprogramming the immunosuppressive TME. This could be reflected in the upregulation of *Batf* and *Irf4* and downregulation of *Egr2* and *Cd200r1* (Fig. 5d, e)[26,27]. Although these genes play multiple roles in cancer immunity[25], recent studies uncover their functions of ameliorating T cell exhaustion[26,27]. For example, the cooperation of *Batf* and *Irf4* is reported to counter $CD8^+$ T cell exhaustion and promote their survival in melanoma tissues[26]. Moreover, *Egr2* is believed to promote the exhaustion of melanoma-infiltrating $CD8^+$ T cells and stabilize the exhausted state via regulating a series of genes including *Cd200r1*[27]. All these data suggest that CATCH treatment has the potential to reduce the $CD8^+$ T cell exhaustion and enhance their antitumor activities.

Intratumoural (i.t.) administration of immunotherapeutic agents can improve their in situ bioavailability and, thus, the therapeutic efficiency[28]. For instance, in comparison with intravenous (i.v.) administration of CD40 Ab, i.t. administration can greatly relieve systemic toxicity while remain antitumor effects[29,30]. Recently, data from the first-in-human study have also showed the therapeutic potential of repeated i.t. administration of CD40 Ab[31]. Yet, the complexity of CATCH treatment regimen needs to be considered for future clinical translation. Although image-guided technologies have been applied in deep tumoral lesion injections[32], repeated administrations of this treatment regimen should be further optimized to minimize potential side effects and improve patient compliance. Moreover, the therapeutic efficacy can be improved in certain tumors with poor immunogenicity and harsh immunosuppressive TME. For example, the TME in 4T1 tumor is known to recruit myeloid-derived suppressor cells and Treg cells to support the tumor growth and metastasis. Thus, some therapeutics targeting these suppressor cells can be included in further studies[33,34]. Additionally, in the rechallenged and two-tumor mouse models, mice with brain tumors showed lower survival rates than mice with s.c. tumors. This may be explained by the challenges to cross the blood-brain barrier (BBB)[35,36]. The BBB can limit the access of therapeutic proteins and immune cells to brain tumors, leading to inadequate reprogramming of the TME and the CIC[35,36]. Some clinical data show that cytoreductive surgery can improve the therapeutic effects of DC therapy in glioblastoma patients[37,38]. This may be due to a reduction of tumor burden-associated immunosuppression[37,38]. Other clinical results reveal that direct i.t. injection of DCs into brain tumors can prolong patient survival[37,39]. These findings may encourage further investigations on combining CATCH treatment with brain tumor resection or administrating CATCH treatment via i.c. injection.

Supplementary Methods

Cell culture

B16F10, B16F10-Luc2, A20, 4T1, and A375 cell lines were purchased from American Type Culture Collection. B16F10, B16F10-Luc2, and A375 cells were cultured in DMEM with 10% FBS. A20 and 4T1 cells were cultured with RPMI 1640 medium containing 10% FBS. Mouse bone marrow derived dendritic cells (BMDCs) were obtained by adaptation of previous procedures[40]. Briefly, monocytes from mouse bone marrow were cultured in RPMI 1640 medium with 10% FBS, 50 ng/mL mGM-CSF (Shenandoah Biotechnology, 20015) and 50 ng/mL mIL-4 (Shenandoah Biotechnology, 20018). After 6-day culture, suspended cells were purified with $CD11c^+$ beads (Miltenyi Biotec, 130108338). Human dendritic cells were derived from peripheral blood monocytes which were ordered from Lonza. The monocytes were cultured in RPMI 1640 medium with 10% FBS, 50 ng/mL hGM-CSF (Invitrogen, BMS324) and 50 ng/mL hIL-4 (Invitrogen, RIL4I) for 6-days.

Antibodies

CD40-FITC (HM40-3, Invitrogen, 11040285), 1:50 dilution;
CD40L-FITC (39H5, Invitrogen, MA516506), 1:10 dilution;
CD80-FITC (B7-1, Invitrogen, 11080181), 1:200 dilution;
CD86-PE (B7-2, Invitrogen, 12086281), 1:200 dilution;
CD86-FITC (B7-2, Invitrogen, 11086281), 1:400 dilution;
MHC II-APC (AF6-120.1, Invitrogen, 17532080), 1:150 dilution;
pro-form IL-1β-FITC (NJTEN3, Invitrogen, 11711480), 1:200 dilution;
calreticulin-Alexa Fluor 647 (1G6A7, Novus Biologicals, NBP1-47518AF647), 1:100 dilution;
Ki-67-FITC (SolA15, Invitrogen, 11569882), 1:200 dilution;
Granzyme B-FITC (NGZB, Invitrogen, 11889882), 1:400 dilution;
IFN-γ-FITC (XMG1.2, Biolegend, 505806), 1:50 dilution;
TNF-α-FITC (MP6-XT22, Invitrogen,11732181), 1:400 dilution;
CD62L-FITC (MEL-14, Invitrogen,11-0621-81), 1:100 dilution;
CD44-Alexa Fluor 700 (IM7, Invitrogen, 56044182), 1:300 dilution;
CD11c-PE Cy7 (N418, Invitrogen, 25011481), 1:40 dilution;
CD45-Alexa Fluor 700 (30-F11, Invitrogen, 56-0451-82), 1:40 dilution;
F4/80-PE eFluor 610 (BM8, Invitrogen, 61-4801-82), 1:20 dilution;
Ly-6C-eFluor 450 (HK1.4, Invitrogen, 48-5932-82), 1:100 dilution;
CD103-FITC (2E7, Invitrogen, 11-1031-81), 1:50 dilution;
CD11b-Pacific Blue (M1/70.15, Invitrogen, RM2828), 1:100 dilution;
CD11b-FITC (M1/70, Invitrogen, 11-0112-81), 1:100 dilution;
CD3e-PE (145-2C11, BD Bioscience, 553063), 1:40 dilution;
CD152-PE Cy7 (UC10-4B9, Invitrogen, 25-1522-80), 1:40 dilution;
CD279-FITC (J43, Invitrogen, 11-9985-81), 1:50 dilution;
CD4-Pacific Blue (RM4-5, Invitrogen, MCD0428), 1:100 dilution;
CD8a-APC eFluor 780 (53-6.7, Invitrogen, 47-0081-80), 1:40 dilution.

Flow cytometry gating

The gating strategies were based on previously reported methods[40,41].

B16F10 cells: $CD45^-$

Macrophages: $CD45^+$, $CD11b^+$, $F4/80^+$

Conventional type 1 dendritic cells (cDC1s): $CD45^+$, $F4/80^-$, $Ly6C^-$, MHC II^+, $CD11c^+$, $CD103^+$

Conventional type 2 dendritic cells (cDC2s): $CD45^+$, $F4/80^-$, $Ly6C^-$, MHC II^+, $CD11c^+$, $CD11b^+$

$CD4^+$ T cells: $CD45^+$, $CD3e^+$, $CD4^+$, $FoxP3^-$

Regulatory T cells: $CD45^+$, $CD3e^+$, $CD4^+$, $FoxP3^+$

$CD8^+$ T cells: $CD45^+$, $CD3e^+$, $CD8a^+$

Effector memory T cells: $CD45^+$, $CD3e^+$, $CD8a^+$, $CD44^{hi}$, $CD62L^{lo}$

Central memory T cells: $CD45^+$, $CD3e^+$, $CD8a^+$, $CD44^{hi}$, $CD62L^{hi}$

Tissue dissociation and mononuclear cell isolation

Tumoral tissues were dissociated using mouse tumor dissociation kit (Miltenyi Biotec, 130096730). Spleens and tumor draining lymph nodes were dissociated by mouse spleen dissociation kit (Miltenyi Biotec, 130095926). Mononuclear cells in tumoral tissues and the blood were isolated by Ficoll-Paque density gradient media.

Cellular uptake and endosomal escape

Cells were cultured in a 24-well plate with 10^5 cells/well overnight. Next, the cells were incubated with LNPs encapsulating Alexa-Fluor 647-labeled RNA for 3 h. The cellular uptake was measured by flow cytometry. The endocytic mechanisms of LNPs were evaluated via incubation with different endocytic inhibitors during cellular uptake experiments[42,43]. In endosomal escape assay[42], 2×10^4 cells were seeded in each chamber of an imaging dish (Ibidi, 80416). The cells were then incubated with calcein, LNPs encapsulating Alexa-Fluor 647-labeled RNA, or LysoTracker Red DND-99 for 1 h. After washed by PBS, cells were lively observed under Nikon A1R Live Cell Imaging Confocal Microscope. The co-localization was analysed with NIS-Elements AR 5.20.00.

Tumor models and treatment regimens

C57BL/6, $Batf3^{-/-}$, and BALB/c mice (male and female, 6-8 weeks) were purchased from the Jackson Laboratory and housed in The Ohio State University. $CD40^{-/-}$ mice and *Pmel-1* TCR transgenic mice were purchased from the Jackson Laboratory and housed in The Icahn School of Medicine at Mount Sinai. All mouse studies were approved by the Institutional Animal Care and Use Committee (IACUC) at The Ohio State University (2014A00000106) and The Icahn School of Medicine at Mount Sinai (IPROTO202200000134), and complied with local, state, and federal regulations. In this study, up to 5 mice were housed in each cage under a barrier environment with the condition (~20°C, ~45% humidity, and 12 light/12 dark cycle). Mouse experiments were carried out based on reported methods[35,40,44].

For one-side subcutaneous (s.c.) tumor model, about 1×10^5 B16F10 cells, 2×10^5 B16F10-Luc2 cells, 5×10^6 A20 cells, or 1×10^6 4T1 cells were s.c. inoculated on the right flank. On day 7 post tumor inoculation, mice with tumor size about or over 0.5 cm of the largest diameter were randomly separated into different groups. For two-side s.c. tumor model, about 1×10^5 B16F10 cells were s.c. inoculated on the right flank. On day 5 post tumor inoculation on the right flank, about 1×10^5 B16F10 cells were s.c. administrated on the left flank. On day 7 post tumor inoculation on the right flank, mice with tumor size about or over 0.5 cm of the largest diameter

were randomly separated into different groups. For skin + brain two tumor model, about 2×10^5 B16F10-Luc2 cells were s.c. administrated on the right flank. On day 5 post tumor inoculation on the right flank, about 1×10^4 B16F10-Luc2 cells were intracranially (i.c.) injected with a depth of 3 mm. The injection site was 2 mm lateral and 1 mm anterior to the sagittal suture and to the coronal suture, respectively. On day 7 post tumor inoculation on the right flank, mice with tumor size about or over 0.5 cm of the largest diameter were randomly separated into different groups. For s.c. tumor rechallenge, on day 45 post tumor inoculation, about 1×10^5 B16F10 cells were s.c. injected on the left flank of completely responded mice. For brain tumor rechallenge, on day 45 post tumor inoculation, about 1×10^4 B16F10-Luc2 cells were i.c. injected in completely responded mice. For T cell depletion tumor models, 1×10^5 B16F10 cells were s.c. injected into the right flank of mice. On day 6 post tumor inoculation, mice were intraperitoneally treated with anti-mouse CD8α, anti-mouse CD4, or anti-rat IgG2b isotype antibody. Each antibody was given every 3 days for three doses with 200 μg per injection.

Treatment regimens in this study are as described below. In a single i.t. injection, the doses of CD40 Ab and LNPs were 50 μg and 5 μg, respectively; and the dose of dendritic cells was 2 million. For CD40-LNPs+CD40 Ab treatment, CD40 Ab was i.t. administrated 6 h post the i.t. injection of CD40-LNPs. For dendritic cells+CD40 Ab treatment, CD40 Ab was i.t. administrated 1 h post the i.t. injection of dendritic cells. For CD40-LNPs+CD40L-LNPs treatment, CD40-LNPs were i.t. administrated 18 h post the i.t. injection of CD40L-LNPs. For CD40L- or FLuc-LNPs+CD40-BMDCs treatment, CD40-BMDCs were i.t. administrated 18 h post the i.t. injection of CD40L- or FLuc-LNPs.

Chemical Synthesis of dianhydrohexitols-derived lipids

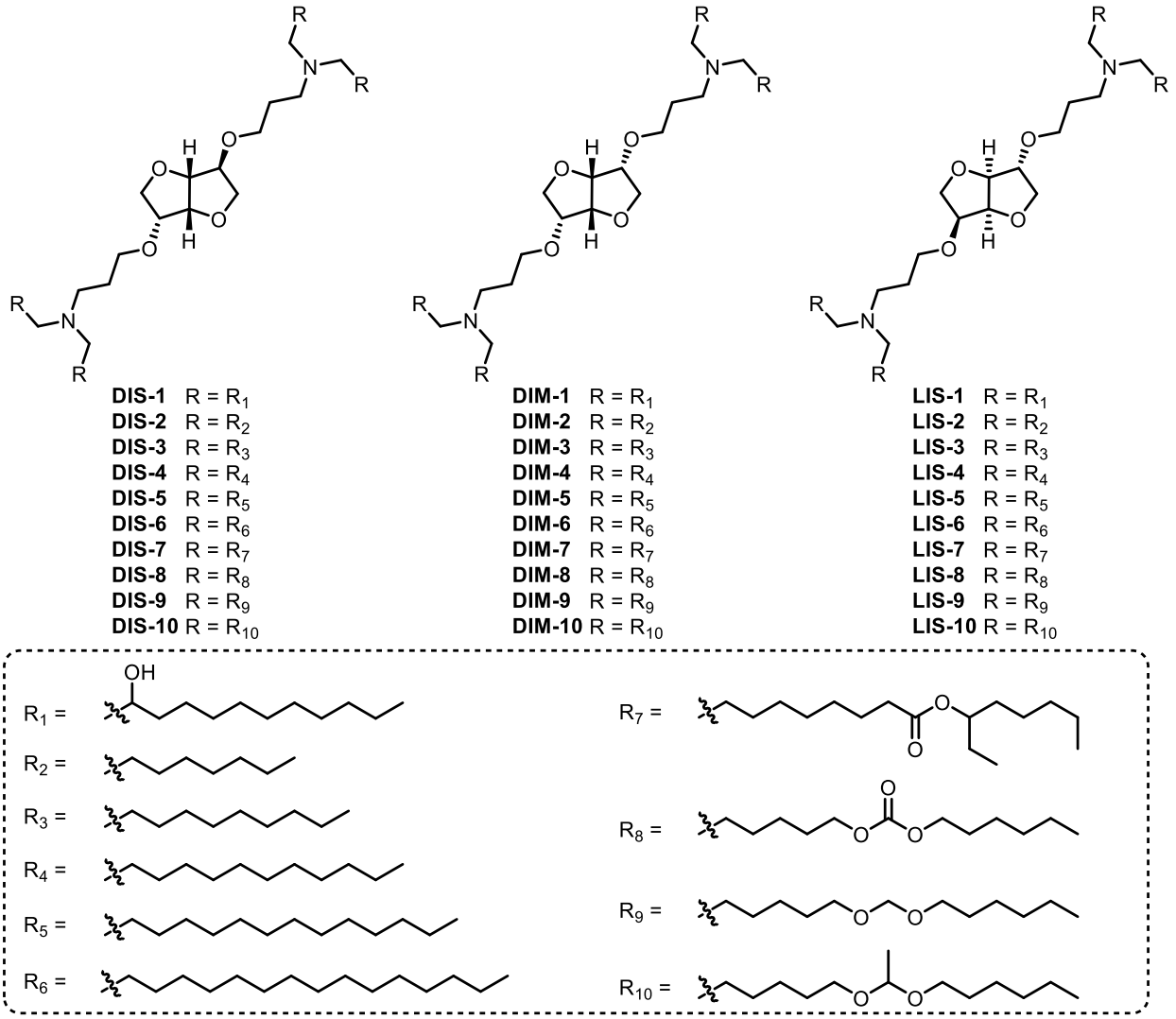

Chemical Structures of dianhydrohexitols-derived ionizable lipids

Synthesis of aldehydes

Aldehydes were synthesized according to previously reported procedures[45,46].

Synthesis of sugar alcohol-derived diamines

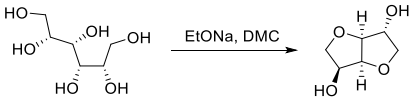

To a solution of L-isosorbide (2.0 g, 10.98 mmol) and Diethyl Carbonate (DMC) (3.96 g, 43.9 mmol) in 12 mL of MeOH was added EtONa (75 mg, 1.1 mmol), the resulting mixture was allowed to reflux for 48 h. Then the reaction was stopped, cooled at room temperature, and diethyl ether

(15 mL) was added to the mixture. The reaction mixture was then filtered through a pad of Celite and the solvent evaporated. Finally, the product was purified by silica gel chromatography using dichloromethane/methanol (9:1) as eluent, 1.2 g of desired product was obtained as a white solid, yield 75%. ^{1}H NMR (400 MHz, Deuterium Oxide) δ 4.68 (t, *J* = 4.7 Hz, 1H), 4.52 (d, *J* = 4.3 Hz, 1H), 4.43 (td, *J* = 6.9, 5.0 Hz, 1H), 4.36 (d, *J* = 3.2 Hz, 1H), 4.02 – 3.94 (m, 2H), 3.90 (dd, *J* = 10.5, 3.2 Hz, 1H), 3.52 (dd, *J* = 9.1, 7.4 Hz, 1H). ^{13}C NMR (75 MHz, Deuterium Oxide) δ 87.33, 81.40, 75.46, 75.07, 71.76, 71.09. MS (ESI, *m/z*): $[M+H]^+$ calcd. For $C_6H_{11}O_4$, 147.1; found: 147.1.

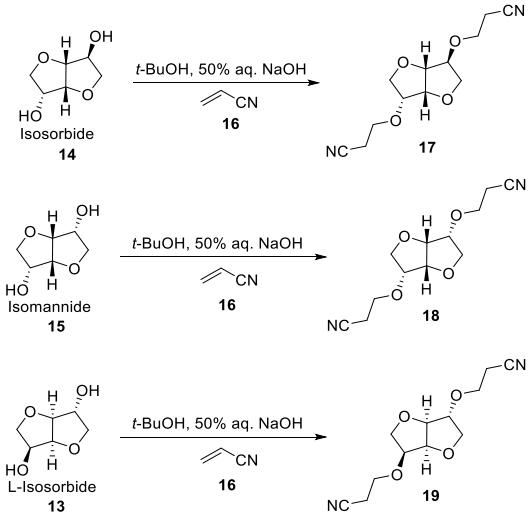

Dicyanoethylation of diols were carried out according to a previously reported method[47]. To a solution of diol (7.3 g, 50 mmol) in *tert*-butanol and 50% aqueous NaOH solution (2.0 g, 0.5mol%) was add acrylonitrile **16** (7.96 g, 150 mmol) dropwise over 30 min at 60 °C. The reaction was continued over a total period of 6 hours. Tert-Butanol and the excess acrylonitrile were removed via rotate evaporation under reduced pressure. The residue was dissolved in 100 mL of DCM, unreacted isosorbide and monocyanoethylated isosorbide were removed by triple water washing. The organic layer was dried over anhydrous Na_2SO_4, the solution was filtered and the solvent was removed under reduced pressure. The residue was purified by silica gel chromatography (0%–100% Hexane in Dichloromethane) to corresponding product as a yellow oil.

Compound **17**: yield 70.5%. ^{1}H NMR (400 MHz, DMSO-d_6) δ 4.60 (t, *J* = 4.8 Hz, 1H), 4.42 (dt, *J* = 4.4, 1.2 Hz, 1H), 4.06 (td, *J* = 6.4, 4.8 Hz, 1H), 4.02 – 3.98 (m, 1H), 3.89 – 3.72 (m, 4H), 3.67 – 3.60 (m, 3H), 3.47 (dd, *J* = 8.8, 6.8 Hz, 1H), 2.78 – 2.72 (m, 4H). MS (ESI, *m/z*): $[M+Na]^+$ calcd. For $C_{12}H_{17}N_2O_4$, 275.1002; found: 275.1007.

Compound **18**: yield 68%. ^{1}H NMR (300 MHz, DMSO-d_6) δ 4.52 (dt, *J* = 4.7, 2.4 Hz, 2H), 4.07 (tdd, *J* = 8.0, 3.6, 1.6 Hz, 2H), 3.89 (dd, *J* = 8.5, 6.7 Hz, 2H), 3.79 – 3.73 (m, 1H), 3.71 (d, *J* = 6.1 Hz, 1H), 3.62 (ddd, *J* = 9.7, 6.5, 5.7 Hz, 2H), 3.50 (t, *J* = 8.2 Hz, 2H), 2.75 (ddd, *J* = 6.6, 5.7, 1.1 Hz, 4H). MS (ESI, *m/z*): $[M+Na]^+$ calcd. For $C_{12}H_{17}N_2O_4$, 275.1; found: 275.1.

Compound **19**: yield 93%. ^{1}H NMR (300 MHz, DMSO-d_6) δ 4.61 (t, *J* = 4.8 Hz, 1H), 4.43 (dt, *J* = 4.8, 0.9 Hz, 1H), 4.07 (td, *J* = 6.6, 4.8 Hz, 1H), 4.03 – 3.97 (m, 1H), 3.90 – 3.72 (m, 4H), 3.70 – 3.59 (m, 3H), 3.48 (dd, *J* = 8.7, 6.6 Hz, 1H), 2.82 – 2.71 (m, 4H). ^{13}C NMR (75 MHz, DMSO-d_6) δ 120.07, 120.06, 86.42, 84.49, 80.89, 80.46, 73.44, 70.70, 65.47, 64.54, 19.19, 19.14. MS (ESI, *m/z*): $[M+Na]^+$ calcd. For $C_{12}H_{17}N_2O_4$, 275.1; found: 275.0.

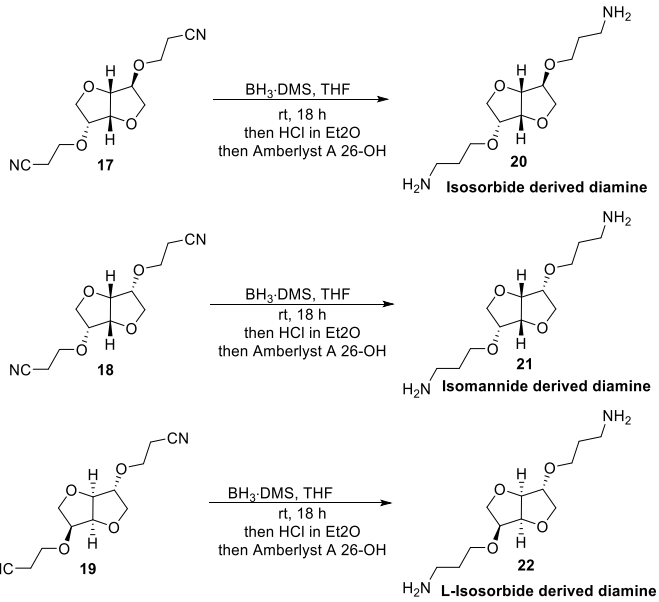

Diamines were synthesized according to methods reported previously[48]. To a solution of BH_3·THF complex in THF (2.0 M, 29.7 mL, 59.4 mmol) was added a solution of dinitrile compound (3.0 g, 11.89 mmol) in THF (25 mL) dropwise over 1 h at room. After the addition was completed, the reaction was stirred for 48 h. Then, methanol (30 mL) was added carefully to quench the reaction, during which hydrogen gas evolved vigorously. After stirring for 3 h, the solvent was removed under reduced pressure, then 40 mL of THF was added to dissolve the residue followed by the addition of hydrochloric acid in diethyl ether solution (2.0 M, 29.7 mL) dropwise upon which a white precipitate formed. The suspension was then filtered to give the crude diamine·HCl salt as a white powder. Then the diamine·2HCl salt was dissolved in deionized water (30 mL) to give a light yellow solution. To this solution freshly washed Amberlyst A 26-OH (17 g) was added. The resulting suspension was sonicated in an ultrasonic bath for 1.5 h at 30 °C. The suspension was filtered through a pad of Celite and the resin was washed thoroughly with water (3 × 4 mL). The combined clear colorless solutions were evaporated to dryness using a rotary evaporator (or freeze-dried) to afford the extended diamine as a light yellow oily liquid.

Isosorbide derived diamine **20**: yield 70%. ^{1}H NMR (300 MHz, Methanol-d_4) δ 4.64 (t, J = 4.5 Hz, 1H), 4.54 – 4.45 (m, 1H), 4.11 – 4.00 (m, 1H), 3.98 – 3.84 (m, 4H), 3.80 – 3.69 (m, 1H), 3.66 – 3.43 (m, 4H), 2.86 – 2.61 (m, 4H), 1.83 – 1.67 (m, 4H). HRMS (ESI, *m/z*): $[M+H]^+$ calcd. For $C_{12}H_{25}N_2O_4$, 261.1809; found: 261.1819.

Isomannide derived diamine **21**: yield 68%. HRMS (ESI, *m/z*): $[M+H]^+$ calcd. For $C_{12}H_{25}N_2O_4$, 261.1809; found: 261.1817.

L-Isosorbide derived diamine **22**: yield 71%. ^{1}H NMR (400 MHz, Methanol-d_4) δ 4.67 (t, J = 4.4 Hz, 1H), 4.56 – 4.54 (m, 1H), 4.13 – 4.10 (m, 1H), 3.98 – 3.92 (m, 2H), 3.92 – 3.86 (m, 2H), 3.78 – 3.68 (m, 1H), 3.68 – 3.50 (m, 4H), 2.94 – 2.71 (m, 4H), 1.85 – 1.73 (m, 4H). MS (ESI, *m/z*): $[M+H]^+$ calcd. For $C_{12}H_{25}N_2O_4$, 261.2; found: 261.2.

Synthesis of β-aminoalcohols

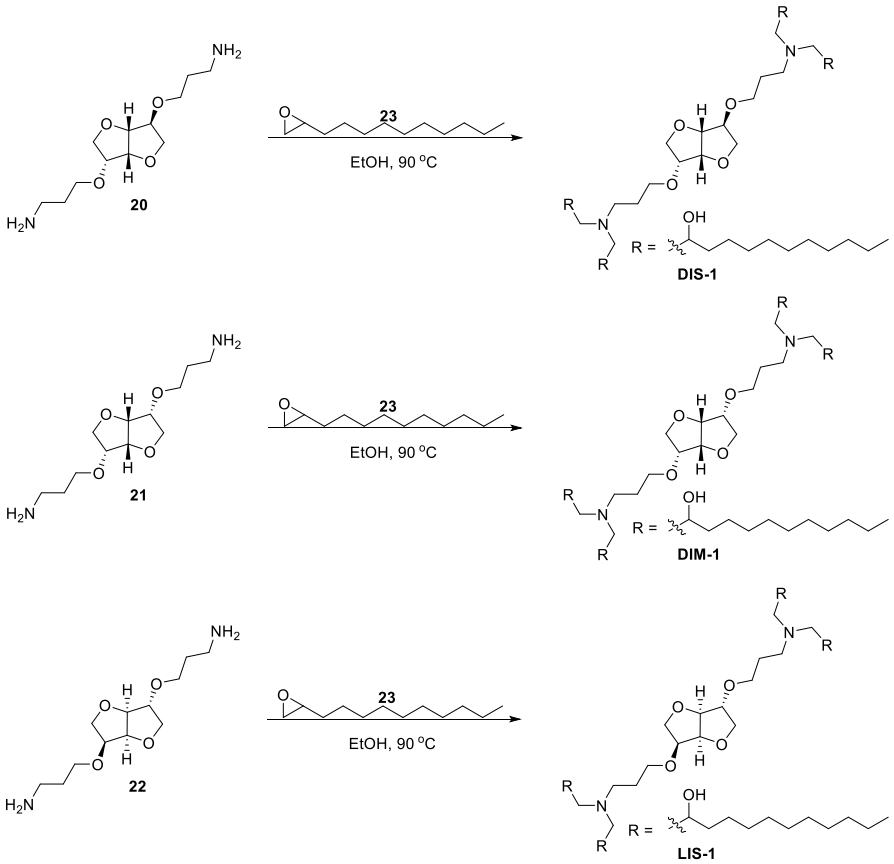

To a solution of diamine (52 mg, 0.2 mmol) in 2 mL of dry EtOH was added epoxide **23** (184 mg, 1.0 mmol). Then the mixture was warmed to 90 °C and kept stirring for 12 h. TLC showed totally consumed of A, EtOH was removed under reduced pressure. The residue was purified via silica gel chromatography (0%–100% [mixture of 3% NH4OH, 22% MeOH in dichloromethane] in dichloromethane) to give desire products.

DIS-1: yield 61.2%. ^{1}H NMR (300 MHz, Chloroform-*d*) δ 4.66 – 4.60 (m, 1H), 4.51 (d, *J* = 3.9 Hz, 1H), 3.95 (qd, *J* = 7.5, 3.9 Hz, 5H), 3.88 – 3.05 (m, 11H), 2.97 – 2.05 (m, 12H), 1.82 – 1.60 (m, 4H), 1.50 – 1.19 (m, 72H), 0.99 – 0.78 (m, 12H). HRMS (ESI, *m/z*): $[M+H]^+$ calcd. For $C_{60}H_{121}N_2O_8$, 997.9118; found: 997.9118.

DIM-1: yield 69.2%. ^{1}H NMR (300 MHz, Chloroform-*d*) δ 4.56 (dd, *J* = 4.5, 2.7 Hz, 2H), 4.11 – 3.89 (m, 4H), 3.89 – 3.49 (m, 9H), 3.49 – 3.23 (m, 5H), 2.86 – 2.14 (m, 12H), 1.85 – 1.65 (m, 4H), 1.50 – 1.17 (m, 72H), 0.91 – 0.80 (m, 12H). MS (ESI, *m/z*): $[M+H]^+$ calcd. For $C_{60}H_{121}N_2O_8$, 997.9; found: 998.0.

LIS-1: yield 38.1%. ^{1}H NMR (300 MHz, Chloroform-*d*) δ 4.67 – 4.61 (m, 1H), 4.55 – 4.39 (m, 1H), 4.03 – 3.80 (m, 5H), 3.55 (tdd, *J* = 34.4, 30.2, 12.9, 6.2 Hz, 12H), 2.90 – 2.08 (m, 12H), 1.86 – 1.61 (m, 4H), 1.47 – 1.19 (m, 72H), 0.87 (t, *J* = 6.5 Hz, 12H). MS (ESI, *m/z*): $[M+H]^+$ calcd. For $C_{60}H_{121}N_2O_8$, 997.9; found: 998.0.

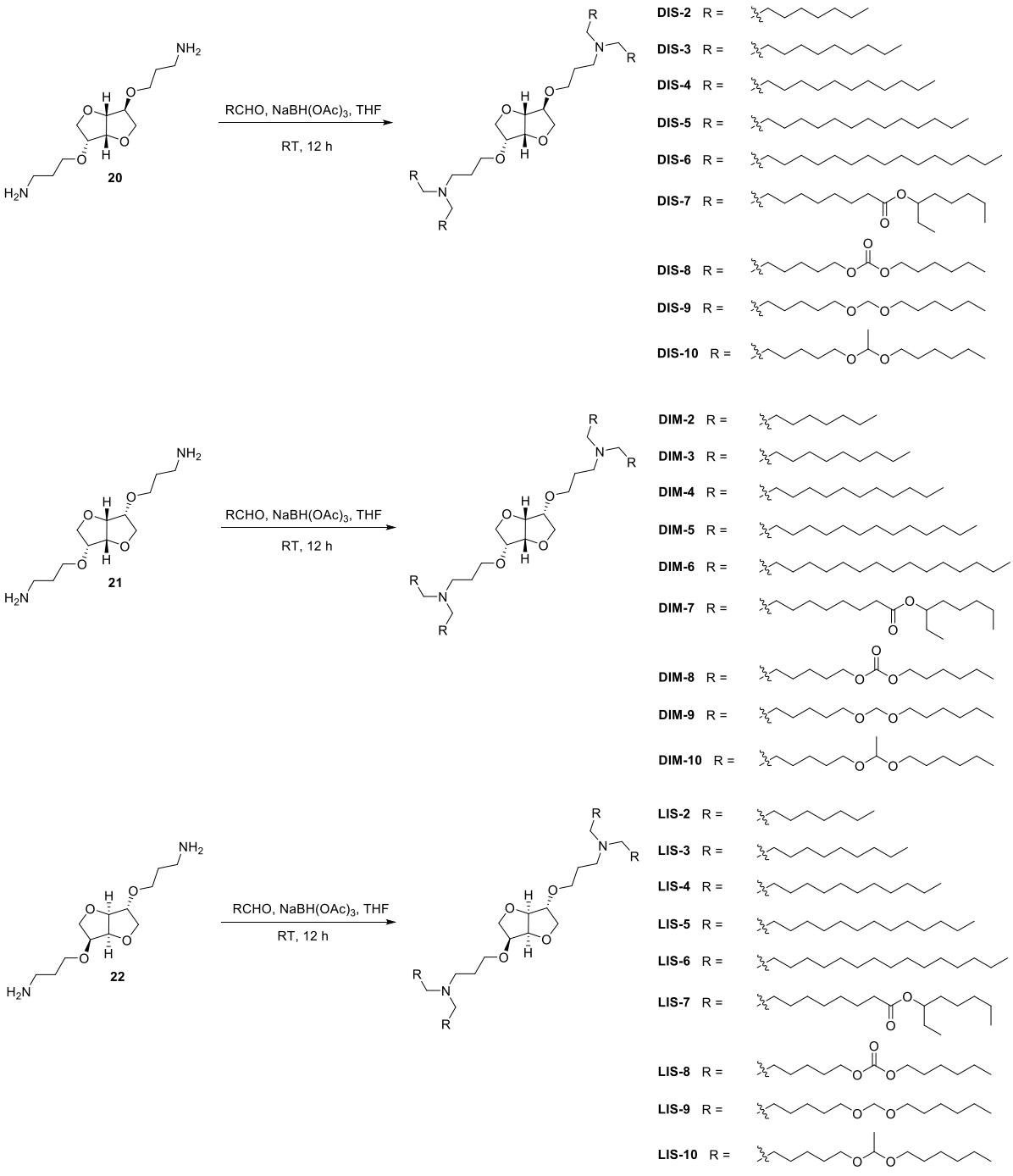

General synthetic procedure for the reductive amination of diamines

To a solution of diamine (52 mg, 0.2 mmol) in THF (4 mL) was added aldehyde (1.0 mmol), the mixture was kept stirring for 30 min at RT. Then $NaBH(OAc)_3$ (254 mg, 1.2 mmol) was added to the above solution, and the resulting mixture was stirred for 12 h. Aq. $NaHCO_3$ solution (15 mL) was added to quench the reaction. The aqueous solution was extracted with DCM (15 mL*3 times), the organic phase was combined and dried over anhydrous Na_2SO_4, filtered and concentrated under

reduced pressure. The residue was purified via silicon gel chromatography (0%–100% [mixture of 3% NH_4OH, 22% MeOH in Dichloromethane] in Dichloromethane) to give desired compounds.

Compound **DIS-2**: yield 37.0%. ^{1}H NMR (300 MHz, Chloroform-*d*) δ 4.60 (t, *J* = 4.2 Hz, 1H), 4.48 (d, *J* = 4.2 Hz, 1H), 4.02 – 3.84 (m, 5H), 3.68 (dt, *J* = 9.3, 6.6 Hz, 1H), 3.62 – 3.33 (m, 4H), 2.63 – 2.18 (m, 12H), 1.79 – 1.60 (m, 4H), 1.49 – 1.15 (m, 48H), 0.88 (t, *J* = 6.6 Hz, 12H). MS (ESI, *m/z*): $[M+H]^+$ calcd. For $C_{44}H_{89}N_2O_4$, 709.7; found: 709.9.
Compound **DIS-3**: yield 37.0%. ^{1}H NMR (300 MHz, Chloroform-*d*) δ 4.60 (t, *J* = 4.2 Hz, 1H), 4.48 (d, *J* = 4.2 Hz, 1H), 4.03 – 3.87 (m, 5H), 3.75 – 3.62 (m, 1H), 3.62 – 3.38 (m, 4H), 2.61 – 2.40 (m, 4H), 2.40 – 2.25 (m, 8H), 1.76 – 1.65 (m, 4H), 1.48 – 1.15 (m, 64H), 0.88 ((t, *J* = 6.6 Hz, 12H). MS (ESI, *m/z*): $[M+H]^+$ calcd. For $C_{52}H_{105}N_2O_4$, 821.8; found: 821.9.
Compound **DIS-4**: yield 49.3%. ^{1}H NMR (300 MHz, Chloroform-*d*) δ 4.59 (t, *J* = 4.5 Hz, 1H), 4.48 (d, *J* = 4.2 Hz, 1H), 4.01 – 3.85 (m, 5H), 3.72 – 3.65 (m, 1H), 3.62 – 3.37 (m, 4H), 2.60 – 2.28 (m, 12H), 1.83 – 1.55 (m, 4H), 1.48 – 1.32 (m, 8H), 1.30 – 1.17 (s, 72H), 0.97 – 0.74 (m, 12H).. MS (ESI, *m/z*): $[M+H]^+$ calcd. For $C_{60}H_{121}N_2O_4$, 933.9321; found: 933.9320.
Compound **DIS-5**: yield 33.0%. ^{1}H NMR (300 MHz, Chloroform-*d*) δ 4.60 (t, *J* = 4.2 Hz, 1H), 4.48 (d, *J* = 4.2 Hz, 1H), 4.02 – 3.85 (m, 5H), 3.72 – 3.64 (m, 1H), 3.62 – 3.38 (m, 4H), 2.54 – 2.25 (m, 12H), 1.79 – 1.61 (m, 4H), 1.50 – 1.15 (m, 96H), 0.98 – 0.81 (m, 12H). MS (ESI, *m/z*): $[M+H]^+$ calcd. For $C_{68}H_{137}N_2O_4$, 1046.1; found: 1046.0.
Compound **DIS-6**: yield 19.1%. ^{1}H NMR (300 MHz, Chloroform-*d*) δ 4.59 (t, *J* = 4.2 Hz, 1H), 4.48 (d, *J* = 4.2 Hz, 1H), 4.02 – 3.85 (m, 5H), 3.72 – 3.65 (m, 1H), 3.63 – 3.41 (m, 4H), 2.73 – 2.30 (m, 12H), 1.84 – 1.65 (m, 4H), 1.50 – 1.35 (m, 8H), 1.35 – 1.17 (m, 104H), 0.92 – 0.80 (m, 12H). MS (ESI, *m/z*): $[M+H]^+$ calcd. For $C_{76}H_{153}N_2O_4$, 1158.2; found: 1158.2.
Compound **DIS-7**: yield 45.7%. ^{1}H NMR (400 MHz, Chloroform-*d*) δ 4.81 (ddd, *J* = 12.4, 6.8, 5.6 Hz, 4H), 4.59 (t, *J* = 4.0 Hz, 1H), 4.48 (d, *J* = 4.2 Hz, 1H), 4.02 – 3.80 (m, 5H), 3.68 (dt, *J* = 9.1, 6.5 Hz, 1H), 3.70 – 3.63 (m, 1H), 3.52 – 3.40 (m, 3H), 2.54 – 2.39 (m, 4H), 2.35 (tt, *J* = 7.2, 3.2 Hz, 8H), 2.28 (t, *J* = 7.6 Hz, 8H), 1.86 – 1.41 (m, 28H), 1.41 – 1.05 (m, 64H), 0.94 – 0.79 (m, 24H). HRMS (ESI, *m/z*): $[M+H]^+$ calcd. For $C_{80}H_{153}N_2O_{12}$, 1334.1418; found: 1334.1404.
Compound **DIS-8**: yield 35.0%. ^{1}H NMR (300 MHz, Chloroform-*d*) δ 4.59 (t, *J* = 4.2 Hz, 1H), 4.47 (d, *J* = 4.2 Hz, 1H), 4.11 (t, *J* = 6.9 Hz, 16H), 4.01 – 3.86 (m, 5H), 3.74 – 3.62 (m, 1H), 3.60 – 3.46 (m, 4H), 2.47 – 2.30 (m, 12H), 1.77 – 1.61 (m, 20H), 1.43 – 1.24 (m, 48H), 1.01 – 0.79 (m, 12H). MS (ESI, *m/z*): $[M+H]^+$ calcd. For $C_{64}H_{121}N_2O_{16}$, 1173.9; found: 1174.0.
Compound **DIS-9**: yield 31.0%. ^{1}H NMR (300 MHz, Chloroform-*d*) δ 4.66 (s, 8H), 4.60 (t, *J* = 4.2 Hz, 1H), 4.48 (d, *J* = 4.2 Hz, 1H), 4.01 – 3.85 (m, 4H), 3.72 – 3.64 (m, 1H), 3.60 – 3.38 (m, 20H), 2.60 – 2.30 (m, 12H), 1.79 – 1.52 (m, 20H), 1.49 – 1.22 (m, 48H), 0.95 – 0.80 (m, 12H). MS (ESI, *m/z*): $[M+H]^+$ calcd. For $C_{64}H_{129}N_2O_{12}$, 1118.0; found: 1118.1.
Compound **DIS-10**: yield 54.5%. ^{1}H NMR (300 MHz, Chloroform-*d*) δ 4.65 (d, *J* = 5.2 Hz, 4H), 4.58 (t, *J* = 4.2 Hz, 1H), 4.47 (d, *J* = 4.2 Hz, 1H), 4.02 – 3.83 (m, 5H), 3.67 – 3.46 (m, 12H), 3.47 – 3.30 (m, 9H), 2.53 – 2.26 (m, 12H), 1.84 – 1.47 (m, 30H), 1.46 – 1.14 (m, 50H), 0.86 (d, *J* = 6.9 Hz, 12H).MS (ESI, *m/z*): $[M+H]^+$ calcd. For $C_{68}H_{137}N_2O_{12}$, 1174.0; found: 1174.2.
Compound **DIM-2**: yield 54.5%. ^{1}H NMR (300 MHz, Chloroform-*d*) δ 4.59 – 4.49 (m, 2H), 4.11 – 3.92 (m, 4H), 3.75 – 3.61 (m, 4H), 3.51 (dt, *J* = 9.0, 6.6 Hz, 2H), 2.48 (td, *J* = 6.9, 2.1 Hz, 4H), 2.43 – 2.33 (m, 8H), 1.76 (p, *J* = 6.9 Hz, 4H), 1.50 – 1.36 (m, 8H), 1.35 – 1.15 (d, *J* = 2.6 Hz, 40H), 0.89 (t, *J* = 6.9 Hz, 12H). MS (ESI, *m/z*): $[M+H]^+$ calcd. For $C_{44}H_{89}N_2O_4$, 709.7; found: 709.8.
Compound **DIM-3**: yield 31.7%. ^{1}H NMR (300 MHz, Chloroform-*d*) δ 4.52 (dd, *J* = 3.0, 1.2 Hz, 2H), 4.07 – 3.93 (m, 4H), 3.75 – 3.58 (m, 4H), 3.49 (dt, *J* = 9.0, 6.6 Hz, 2H), 2.46 (td, *J* = 6.9, 1.8

Hz, 4H), 2.41 – 2.27 (m, 8H), 1.74 (p, *J* = 6.9 Hz, 4H), 1.39 (p, *J* = 6.8, 6.2 Hz, 8H), 1.32 – 1.15 (m, 56H), 0.87 (t, *J* = 6.6 Hz, 12H). MS (ESI, *m/z*): $[M+H]^+$ calcd. For $C_{52}H_{105}N_2O_4$, 821.8; found: 821.9.

Compound **DIM-4**: yield 49.3%. ^{1}H NMR (400 MHz, Chloroform-*d*) δ 4.53 (dt, *J* = 4.4, 2.0 Hz, 2H), 4.08 – 3.94 (m, 4H), 3.72 – 3.60 (m, 4H), 3.49 (dt, *J* = 9.2, 6.8 Hz, 2H), 2.60 – 2.46 (m, 4H), 2.47 – 2.30 (m, 8H), 1.76 (p, *J* = 7.0 Hz, 4H), 1.49 – 1.35 (m, 8H), 1.31 – 1.20 (m, 72H), 0.88 (t, *J* = 6.8 Hz, 12H). HRMS (ESI, *m/z*): $[M+H]^+$ calcd. For $C_{60}H_{121}N_2O_4$, 933.9321; found: 933.9321.

Compound **DIM-5**: yield 22.0%. ^{1}H NMR (300 MHz, Chloroform-*d*) δ 4.52 (d, *J* = 3.0 Hz, 2H), 4.09 – 3.93 (m, 4H), 3.75 – 3.59 (m, 4H), 3.49 (dt, *J* = 9.0, 6.6 Hz, 2H), 2.46 (td, *J* = 6.9, 1.8 Hz, 4H), 2.41 – 2.27 (m, 8H), 1.74 (p, *J* = 6.9 Hz, 4H), 1.50 – 1.15 (m, 96H), 0.88 (t, *J* = 6.6 Hz, 12H). MS (ESI, *m/z*): $[M+H]^+$ calcd. For $C_{68}H_{137}N_2O_4$, 1046.1; found: 1046.0.

Compound **DIM-6**: yield 37.3%. ^{1}H NMR (300 MHz, Chloroform-*d*) δ 4.55 (dd, *J* = 3.3, 1.5 Hz, 2H), 4.10 – 3.93 (m, 4H), 3.74 – 3.58 (m, 4H), 3.49 (dt, *J* = 9.0, 6.6 Hz, 2H), 2.46 (td, *J* = 6.9, 1.8 Hz, 4H), 2.35 (dd, *J* = 8.5, 6.3 Hz, 8H), 1.74 (p, *J* = 6.9 Hz, 4H), 1.45 – 1.15 (m, 112H), 0.88 (t, *J* = 6.6 Hz, 12H). MS (ESI, *m/z*): $[M+H]^+$ calcd. For $C_{76}H_{153}N_2O_4$, 1158.2; found: 1158.0.

Compound **DIM-7**: yield 36.0%. ^{1}H NMR (400 MHz, Chloroform-*d*) δ 4.81 (p, *J* = 6.4 Hz, 4H), 4.53 (d, *J* = 2.8 Hz, 2H), 4.08 – 3.94 (m, 4H), 3.75 – 3.60 (m, 4H), 3.48 (dt, *J* = 9.0, 6.6 Hz, 2H), 2.51 (t, *J* = 7.2 Hz, 4H), 2.39 (t, *J* = 7.6 Hz, 8H), 2.27 (t, *J* = 7.6 Hz, 8H), 1.76 (p, *J* = 6.8 Hz, 4H), 1.66 – 1.46 (m, 24H), 1.45 – 1.35 (m, 8H), 1.33 – 1.19 (m, 56H), 0.91 – 0.82 (m, 24H).

Compound **DIM-8**: yield 32.5%. ^{1}H NMR (300 MHz, Chloroform-*d*) δ 4.52 (d, *J* = 3.0 Hz, 2H), 4.11 (t, *J* = 6.6 Hz, 15H), 4.04 – 3.91 (m, 4H), 3.74 – 3.57 (m, 4H), 3.54 – 3.40 (m, 2H), 2.45 (t, *J* = 7.2 Hz, 4H), 2.35 (t, *J* = 7.2 Hz, 8H), 1.80 – 1.60 (m, 20H), 1.46 – 1.19 (m, 48H), 0.88 (t, *J* = 6.6 Hz, 12H). MS (ESI, *m/z*): $[M+H]^+$ calcd. For $C_{64}H_{121}N_2O_{16}$, 1173.9; found: 1174.0.

Compound **DIM-9**: yield 26.2%. ^{1}H NMR (400 MHz, Chloroform-*d*) δ 4.65 (s, 8H), 4.52 (d, *J* = 3.6 Hz, 2H), 4.10 – 3.90 (m, 4H), 3.69 – 3.61 (m, 4H), 3.53 – 3.45 (m, 18H), 2.55 – 2.30 (m, 12H), 1.80 – 1.65 (m, 4H), 1.56 (p, *J* = 6.8 Hz, 16H), 1.49 – 1.14 (m, 48H), 0.88 (t, *J* = 6.8 Hz, 12H). MS (ESI, *m/z*): $[M+H]^+$ calcd. For $C_{64}H_{129}N_2O_{12}$, 1118.0; found: 1118.2.

Compound **DIM-10**: yield 29.4%. ^{1}H NMR (300 MHz, Chloroform-*d*) δ 4.64 (q, *J* = 5.4 Hz, 4H), 4.51 (d, *J* = 3.0 Hz, 2H), 4.10 – 3.90 (m, 4H), 3.73 – 3.25 (m, 22H), 2.44 (t, *J* = 7.2 Hz, 4H), 2.35 (t, *J* = 7.2 Hz, 8H), 1.80 – 1.65 (m, 4H), 1.54 (p, *J* = 6.9 Hz, 16H), 1.45 – 1.20 (m, 60H), 0.87 (t, *J* = 6.6 Hz, 12H). MS (ESI, *m/z*): $[M+H]^+$ calcd. For $C_{68}H_{137}N_2O_{12}$, 1174.0; found: 1174.3.

Compound **LIS-2**: yield 31.0%. ^{1}H NMR (400 MHz, Chloroform-*d*) δ 4.60 (t, *J* = 4.4 Hz, 1H), 4.48 (d, *J* = 4.4 Hz, 1H), 4.01 – 3.88 (m, 5H), 3.68 (dt, *J* = 9.2, 6.8 Hz, 1H), 3.57 (t, *J* = 8.0 Hz, 1H), 3.53 – 3.45 (m, 3H), 2.55 – 2.32 (m, 12H), 1.81 – 1.65 (m, 4H), 1.45 – 1.35 (m, 8H), 1.33 – 1.20 (s, 40H), 0.87 (t, *J* = 6.8 Hz, 12H). MS (ESI, *m/z*): $[M+H]^+$ calcd. For $C_{44}H_{89}N_2O_4$, 709.7; found: 709.8.

Compound **LIS-3**: yield 29.2%. ^{1}H NMR (400 MHz, Chloroform-*d*) δ 4.60 (t, *J* = 4.4 Hz, 1H), 4.48 (d, *J* = 4.0 Hz, 1H), 4.03 – 3.86 (m, 5H), 3.69 (dt, *J* = 9.4, 6.4 Hz, 1H), 3.62 – 3.45 (m, 4H), 2.77 – 2.20 (m, 12H), 1.85 – 1.69 (m, 4H), 1.52 – 1.36 (m, 8H), 1.35 – 1.15 (s, 56H), 0.88 (t, *J* = 6.4 Hz, 12H). MS (ESI, *m/z*): $[M+H]^+$ calcd. For $C_{52}H_{105}N_2O_4$, 821.8; found: 822.0.

Compound **LIS-4**: yield 30.3%. ^{1}H NMR (300 MHz, Chloroform-*d*) δ 4.60 (t, *J* = 4.2 Hz, 1H), 4.48 (d, *J* = 4.2 Hz, 1H), 4.00 – 3.85 (m, 5H), 3.68 (dt, *J* = 9.0, 6.3 Hz, 1H), 3.63 – 3.43 (m, 4H), 2.55 – 2.30 (m, 12H), 1.80 – 1.64 (m, 4H), 1.50 – 1.15 (m, 80H), 0.87 (t, *J* = 6.6 Hz, 12H). MS (ESI, *m/z*): $[M+H]^+$ calcd. For $C_{60}H_{121}N_2O_4$, 933.9; found: 934.2.

Compound **LIS-5**: yield 30.6%. ^{1}H NMR (300 MHz, Chloroform-*d*) δ 4.63 (t, *J* = 4.2 Hz, 1H), 4.51 (d, *J* = 4.2 Hz, 1H), 4.14 – 3.85 (m, 5H), 3.80 – 3.65 (m, 1H), 3.64 – 3.45 (m, 4H), 2.70 –

2.30 (m, 12H), 1.89 – 1.62 (m, 4H), 1.55 – 1.40 (m, 8H), 1.40 – 1.15 (m, 88H), 0.90 (d, *J* = 6.3 Hz, 12H). MS (ESI, *m/z*): $[M+H]^+$ calcd. For $C_{68}H_{137}N_2O_4$, 1046.1; found: 1046.3.

Compound **LIS-6**: yield 29.4%. ^{1}H NMR (400 MHz, Chloroform-*d*) δ 4.60 (t, *J* = 4.4 Hz, 1H), 4.48 (d, *J* = 4.4 Hz, 1H), 4.07 – 3.83 (m, 5H), 3.75 – 3.65 (m, 1H), 3.62 – 3.43 (m, 4H), 2.88 – 2.12 (m, 12H), 1.85 – 1.65 (m, 4H), 1.55 – 1.15 (m, 112H), 0.88 (t, *J* = 6.8 Hz, 12H).

Compound **LIS-7**: yield 20.2%. ^{1}H NMR (400 MHz, Chloroform-*d*) δ 4.80 (p, *J* = 6.4 Hz, 4H), 4.59 (t, *J* = 4.4 Hz, 1H), 4.47 (d, *J* = 4.4 Hz, 1H), 4.08 – 3.82 (m, 5H), 3.75 – 3.65 (m, 1H), 3.61 – 3.42 (m, 4H), 2.58 – 2.30 (m, 12H), 2.27 (t, *J* = 7.6 Hz, 8H) 1.77 – 1.48 (m, 28H), 1.42 – 1.18 (m, 64H), 0.92 – 0.82 (m, 24H). MS (ESI, *m/z*): $[M+2H]^{2+}$ calcd. For $C_{80}H_{154}N_2O_{12}$, 667.6; found: 668.0.

Compound **LIS-8**: yield 25.6%. ^{1}H NMR (400 MHz, Chloroform-*d*) δ 4.61 (d, *J* = 4.4 Hz, 1H), 4.50 (d, *J* = 4.4 Hz, 1H), 4.13 (t, *J* = 6.8 Hz, 16H), 4.02 – 3.90 (m, 5H), 3.75 – 3.65 (m, 1H), 3.60 – 3.45 (m, 4H), 2.65 – 2.28 (m, 12H), 1.80 – 1.60 (m, 20H), 1.55 – 1.20 (m, 48H), 0.91 (d, *J* = 6.4 Hz, 12H). MS (ESI, *m/z*): $[M+H]^+$ calcd. For $C_{64}H_{121}N_2O_{16}$, 1173.9; found: 1174.0.

Compound **LIS-9**: yield 26.4%. ^{1}H NMR (400 MHz, Chloroform-*d*) δ 4.66 (s, 8H), 4.59 (t, *J* = 4.0 Hz, 1H), 4.46 (d, *J* = 4.0 Hz, 1H), 4.03 – 3.83 (m, 4H), 3.76 – 3.63 (m, 1H), 3.60 – 3.45 (m, 20H), 2.60 – 2.25 (m, 12H), 1.79 – 1.22 (m, 68H), 0.89 (t, *J* = 6.8 Hz, 12H). MS (ESI, *m/z*): $[M+H]^+$ calcd. For $C_{64}H_{129}N_2O_{12}$, 1118.0; found: 1118.0.

Compound **LIS-10**: yield 25.9%. ^{1}H NMR (400 MHz, Chloroform-*d*) δ 4.65 (q, *J* = 5.2 Hz, 4H), 4.59 (t, *J* = 4.4 Hz, 1H), 4.47 (d, *J* = 4.4 Hz, 1H), 4.03 – 3.84 (m, 5H), 3.67 (dt, *J* = 9.2, 6.4 Hz, 1H), 3.61 – 3.30 (m, 20H), 2.62 – 2.28 (m, 12H), 1.80 – 1.63 (m, 6H), 1.60 – 1.50 (m, 16H), 1.49 – 1.18 (m, 58H), 0.88 (t, *J* = 6.8 Hz, 12H). MS (ESI, *m/z*): $[M+H]^+$ calcd. For $C_{68}H_{137}N_2O_{12}$, 1174.0; found: 1174.1.

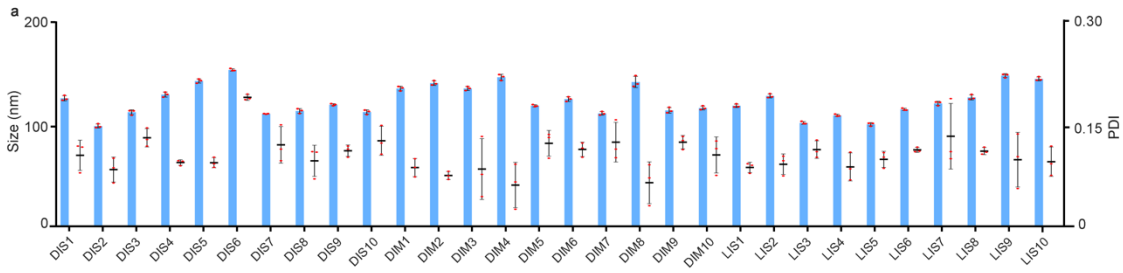

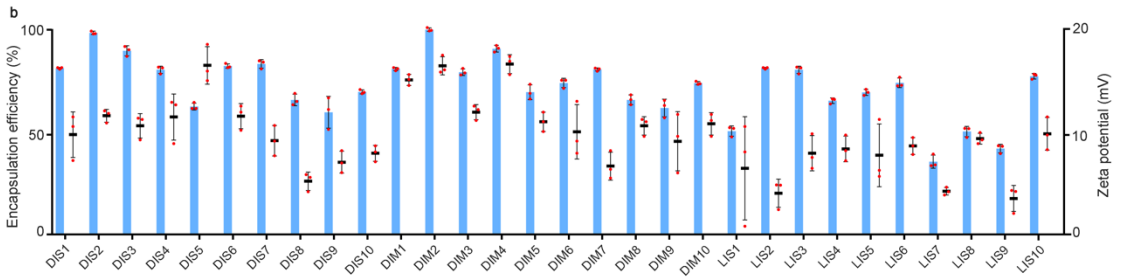

c

L16 $(4)^4$ orthogonal table

Formulation	Factors (molar ratio)			
	Lipid	DOPE	Cholesterol	PEG
A	10	30	40	0.75
B	20	50	20	0.75
C	30	50	40	1
D	40	30	20	0.25
E	10	40	20	1
F	20	20	40	0.25
G	30	20	20	0.75
H	40	40	40	0.5
I	10	20	50	0.5
J	20	40	30	0.75
K	30	40	50	0.25
L	40	20	30	1
M	10	50	30	0.25
N	20	30	50	1
O	30	30	30	0.5
P	40	50	50	0.75

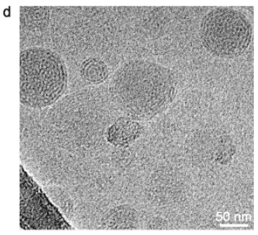

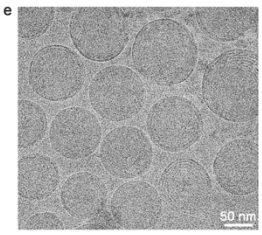

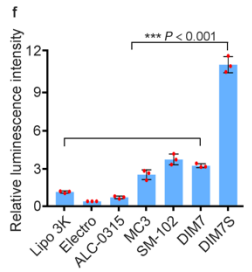

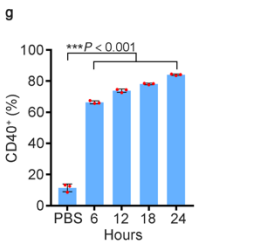

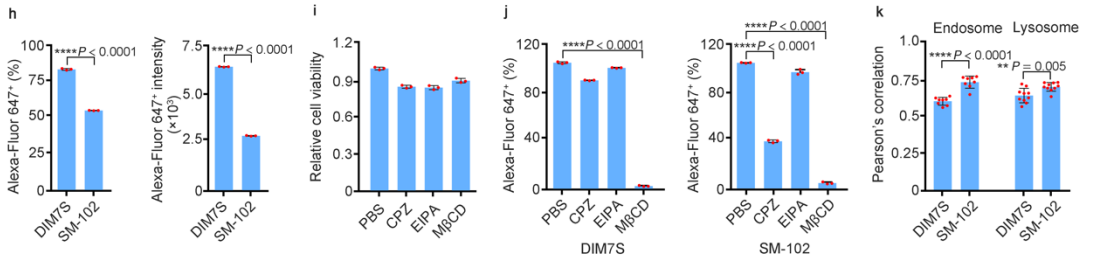

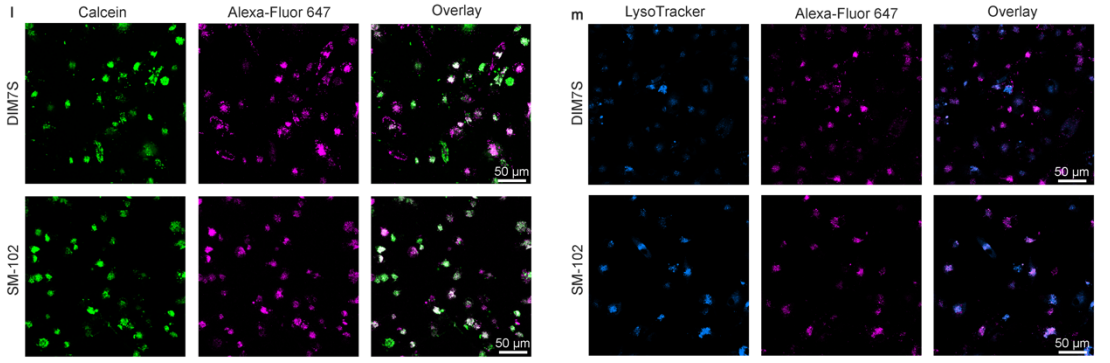

Supplementary Fig. 1. Characterization, optimization, endocytosis, and endosome escape of lipid nanoparticle (LNP)-mRNA formulations. a, Size and polydispersity index (PDI). b, Encapsulation efficiency and zeta potential. c, L16 $(4)^4$ orthogonal table. d, Cryo-TEM image of DIM7S (scale bar = 50 nm). e, Cryo-TEM image of LIS10W (scale bar = 50 nm). f, Relative luminescence intensity from cells treated with electroporation (Electro), ALC-0315, MC3, SM-102, DIM7, and DIM7S to Lipofectamine 3000 (Lipo 3K). g, CD40 expression kinetics mediated by CD40-DIM7S in BMDCs. h, Cellular uptake of DIM7S and SM-102 LNPs. i, Cell viability after treatment by endocytic inhibitors. j, Cellular uptake in the presence of endocytic inhibitors. k, Analysis of colocalization coefficient between LNPs and endosomes or lysosomes. l, m, Confocal imagines of bone marrow derived dendritic cells (BMDCs) incubated with LNPs encapsulating Alexa-Fluor 647 RNA and calcein (l) or LysoTracker (m). Data in d, e, l, and m are representative images from n = 3 independent experiments. Data in a, b and f-j are from n = 3 biologically independent samples. Data in d and e are representative images from n = 3 independent experiments. Data in i are analysed from n = 8 and 10 random views for endosome colocalization and lysosome colocalization, respectively. All data are presented as mean ± s.d. and statistical significance was analysed by two-tailed Student's *t*-test. $^{**}P < 0.01$, $^{****}P < 0.0001$.

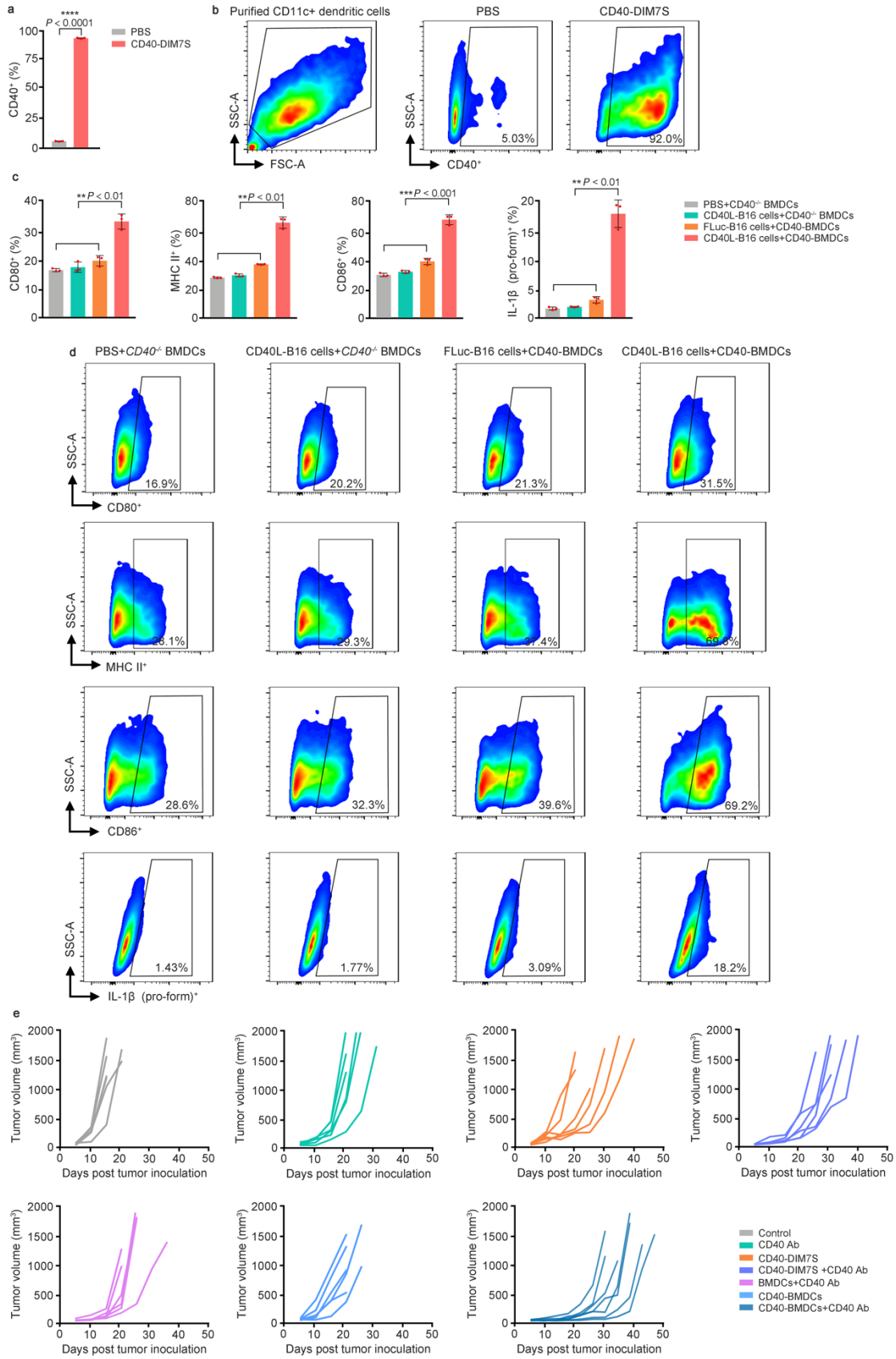
a
****
P < 0.0001
PBS
CD40-DIM7S
CD40+ (%)
b
Purified CD11c+ dendritic cells
PBS
CD40-DIM7S
SSC-A
FSC-A
CD40+
5.03%
92.0%
c
**P < 0.01
***P < 0.001
CD80+ (%)
MHC II+ (%)
CD86+ (%)
IL-1β (pro-form)+ (%)
PBS+CD40-/- BMDCs
CD40L-B16 cells+CD40-/- BMDCs
FLuc-B16 cells+CD40-BMDCs
CD40L-B16 cells+CD40-BMDCs
d
PBS+CD40-/- BMDCs
CD40L-B16 cells+CD40-/- BMDCs
FLuc-B16 cells+CD40-BMDCs
CD40L-B16 cells+CD40-BMDCs
SSC-A
CD80+
16.9%
20.2%
21.3%
31.5%
MHC II+
29.3%
CD86+
28.6%
32.3%
39.6%
69.2%
IL-1β (pro-form)+
1.43%
1.77%
3.09%
18.2%
e
Tumor volume (mm3)
Days post tumor inoculation
Control
CD40 Ab
CD40-DIM7S
CD40-DIM7S +CD40 Ab
BMDCs+CD40 Ab
CD40-BMDCs
CD40-BMDCs+CD40 Ab

Supplementary Fig. 2. CD40 expression-mediated activation on *CD40*$^{-/-}$ BMDCs and tumor volume of individual mice. a, CD40 expression at 24 h. b, Flow cytometry gating schemes. c, Expression of DC activation markers, including CD80, CD86, MHC II, and IL-1β (pro-form). d, Flow cytometry gating schemes. e, Tumor volume of individual mice; n = 7 and 6 for CD40-BMDCs+CD40 Ab group and other groups, respectively. Data in a and c are from n = 3 biologically independent samples and are presented as mean ± s.d. Statistical significance in a and c was analysed by two-tailed Student's *t*-test. $^{**}P < 0.01$, $^{***}P < 0.001$, $^{****}P < 0.0001$.

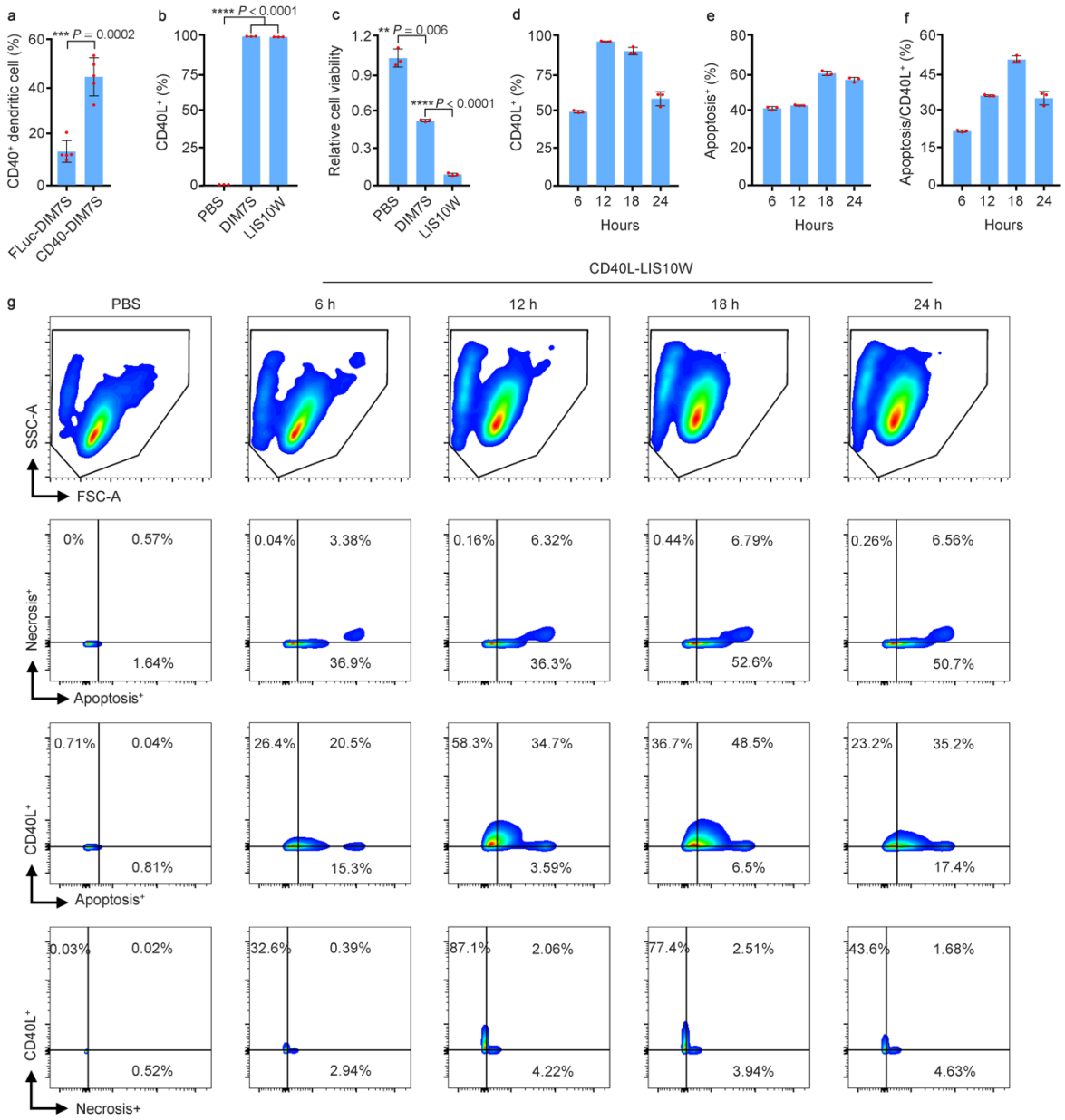

Supplementary Fig. 3. CD40L expression and cytotoxicity induced by LIS10W. a, CD40 expression in tumor-infiltrating DCs mediated by CD40-DIM7S; n = 5 biologically independent mice. b, c, CD40L expression (b) and cell viability (c) induced by CD40L-DIM7S and CD40L-LIS10W in B16F10 melanoma cells. d-f, CD40L expression and apoptosis kinetics mediated by CD40L-LIS10W in B16F10 melanoma cells. g, Flow cytometry gating schemes. Data in b-f are from n = 3 biologically independent samples and are presented as mean ± s.d. Statistical significance was analysed by two-tailed Student's *t*-test. $^{**}P < 0.01$, $^{***}P < 0.001$, $^{****}P < 0.0001$.

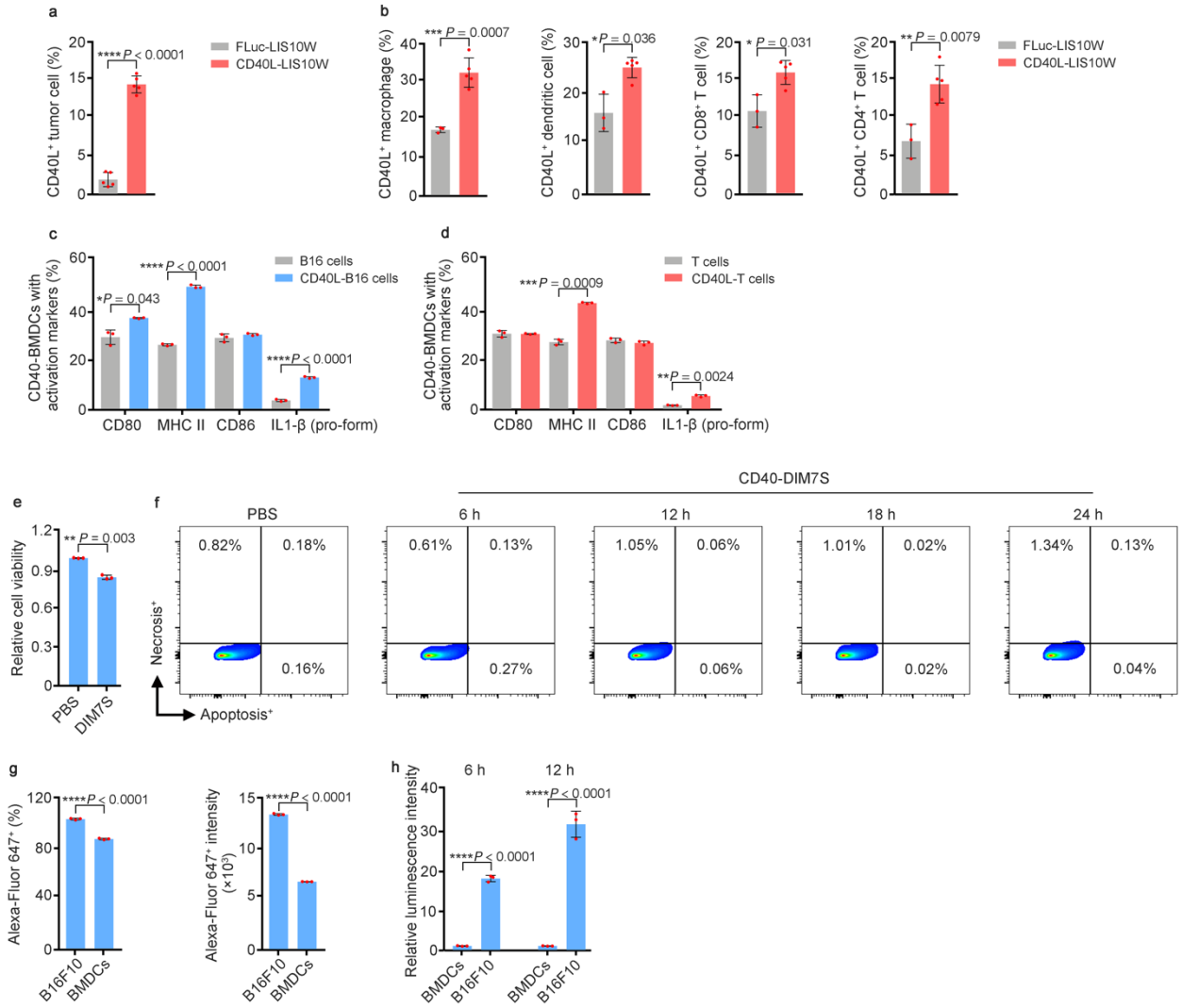

Supplementary Fig. 4. CD40L distribution in tumoral tissues, DC activation via CD40-CD40L interaction, and the differential cytotoxicity induced by DIM7S LNPs in bone marrow derived dendritic cells (BMDCs) and B16F10 melanoma cells. a, In vivo CD40L expression in tumor cells; n = 5 biologically independent mice b, In vivo CD40L expression in immune cells including macrophages, DCs, $CD8^+$ T cells, and $CD4^+$ T cells; n = 3 and 5 biologically independent mice for Fluc-LIS10W and CD40L-LIS10W groups, respectively. c, d, The effects of CD40L expression on tumor cells (c) and T cells (d) on the activation of CD40-BMDCs. e, Cell viability induced by DIM7S in BMDCs. f, Flow cytometry gating schemes. g, Cellular uptake of DIM7S LNPs in BMDCs and B16F10 melanoma cells. h, Luciferase expression mediated by DIM7S LNPs in BMDCs and B16F10 melanoma cells. Data in c, d, e, g and h are from n = 3 biologically independent samples. All data are presented as mean ± s.d. Statistical significance was analysed by two-tailed Student's *t*-test. $*P < 0.05$, $**P < 0.01$, $***P < 0.001$, $****P < 0.0001$.

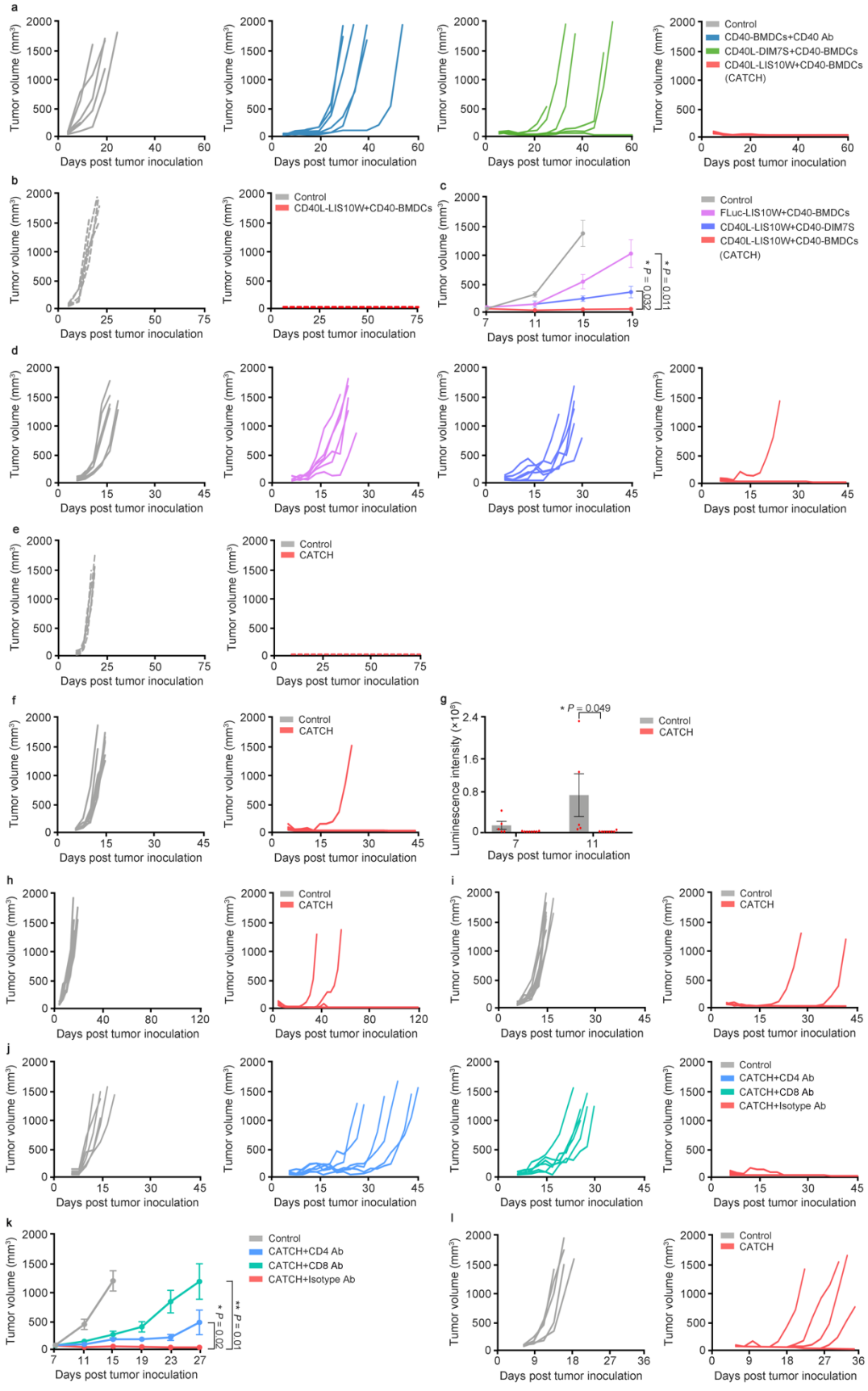
a
b
c
d
e
f
g
h
i
j
k
l
Tumor volume (mm³)
Days post tumor inoculation
Luminescence intensity (×10⁶)
Control
CD40-BMDCs+CD40 Ab
CD40L-DIM7S+CD40-BMDCs
CD40L-LIS10W+CD40-BMDCs (CATCH)
FLuc-LIS10W+CD40-BMDCs
CD40L-LIS10W+CD40-DIM7S
CATCH
CATCH+CD4 Ab
CATCH+CD8 Ab
CATCH+Isotype Ab
* P = 0.049
* P = 0.032
** P = 0.011
* P = 0.02
** P = 0.01

Supplementary Fig. 5. Tumor volume of individual mice. a, Primary tumor volume of individual mice; n = 6. b, Rechallenged s.c. tumor volume of individual mice; n = 5 and 6 for control group and CATCH group, respectively. c, d Tumor volume over time (c) and primary tumor volume of individual mice (d); n = 6. e, Rechallenged s.c. tumor volume of individual mice; n = 5 and 6 for control group and CATCH group, respectively. f, Primary tumor volume of individual mice; n = 9. g, Brain tumor volume over time; n = 5 and 8 for control group and CATCH group, respectively. h, Tumor volume on the treated side of individual mice; n = 8 and 10 for control group and CATCH group, respectively. i, Tumor volume on the treated side of individual mice; n = 10. j, Tumor volume of individual mice; n = 6. k, Tumor volumes over time; n = 6. l, Tumor volume of individual mice; n = 6. Data in c, g and k are presented as mean ± s.e.m. and statistical significance was analysed by two-tailed Student's *t*-test. $*P < 0.05$, $**P < 0.01$.

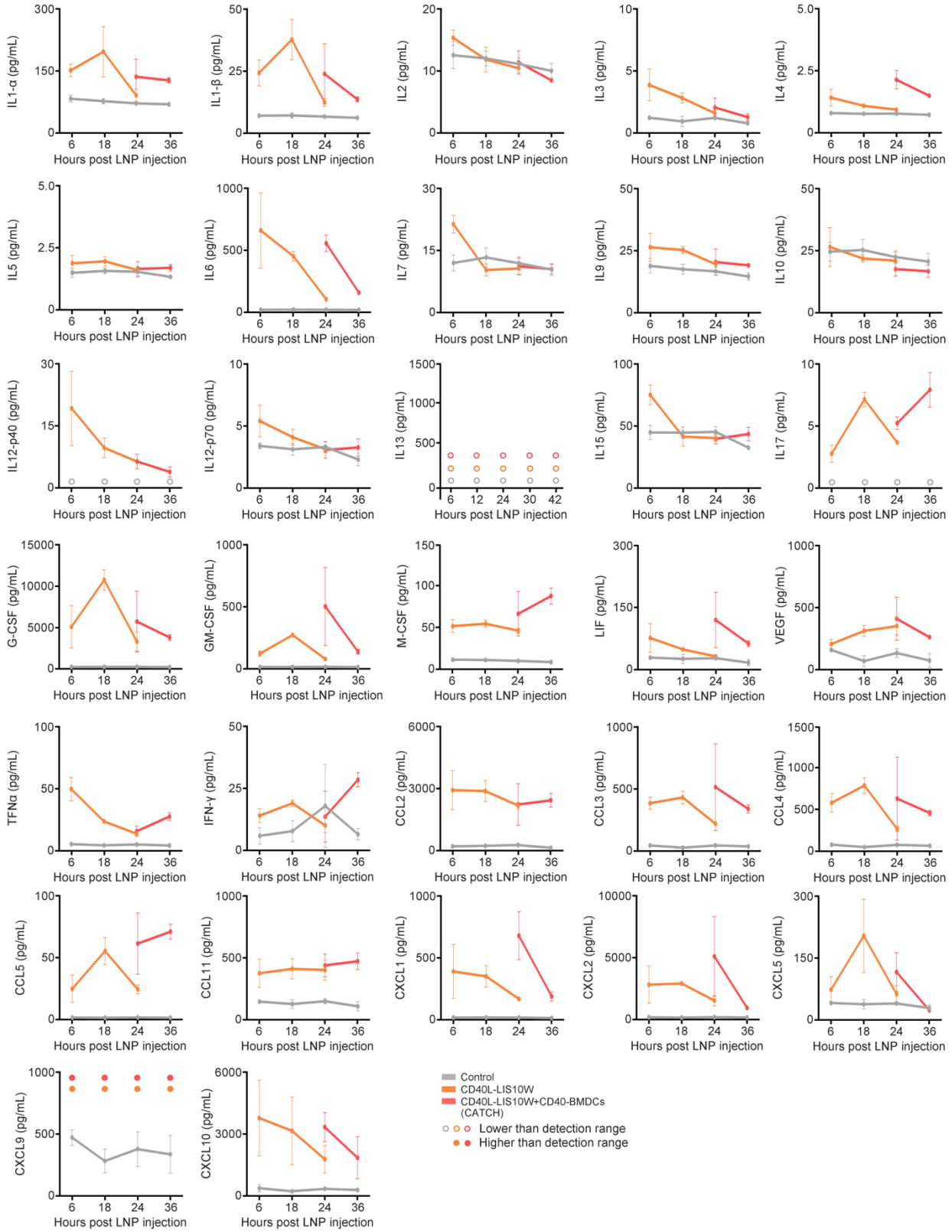

Supplementary Fig. 6. Dynamic expression of cytokines and chemokines in mouse melanoma tissues; n = 5 biologically independent mice. All data are presented as mean ± s.d.

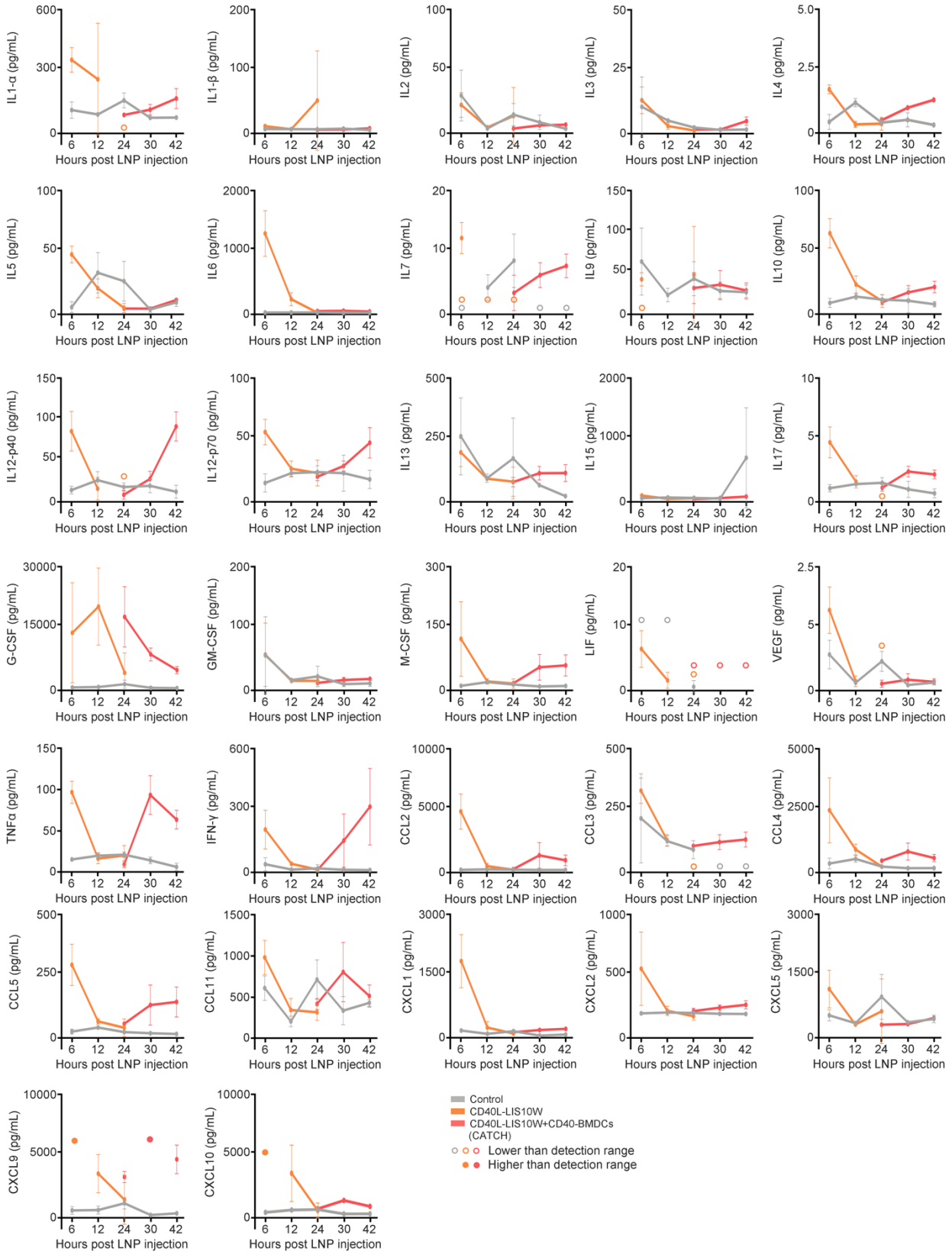

Supplementary Fig. 7. Dynamic expression of cytokines and chemokines in mouse blood; n = 5 biologically independent mice. All data are presented as mean ± s.d.

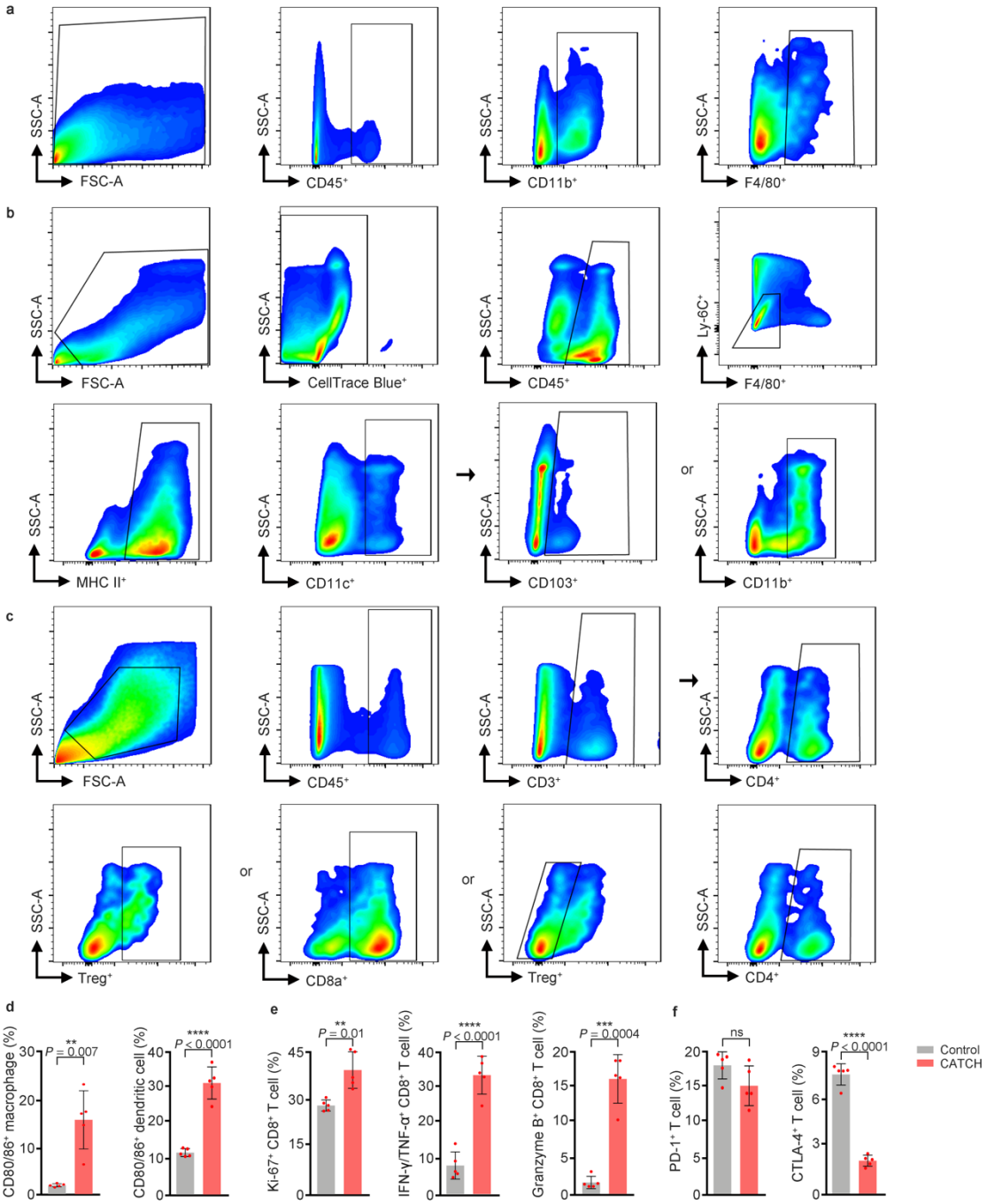

Supplementary Fig. 8. Flow cytometry gating schemes and activation markers of tumor-infiltrating immune cells. a, Flow cytometry gating schemes of macrophages. b, Flow cytometry gating schemes of conventional type 1 and type 2 dendritic cells (cDC1s and cDC2s). c, Flow cytometry gating schemes of $CD4^+$, $CD8^+$, and regulatory T cells. d, Percentage of activated macrophages and DCs in tumoral tissues; n = 5 biologically independent mice. e, Percentage of primed $CD8^+$ T cells in tumoral tissues; n = 5 biologically independent mice. f, Percentage of T cells expressing inhibitory receptors; n = 5 biologically independent mice. Data in d-f are presented as mean ± s.d. and statistical significance was analysed by two-tailed Student's *t*-test. $^{**}P < 0.01$, $^{***}P < 0.001$, $^{****}P < 0.0001$, ns, not significant.

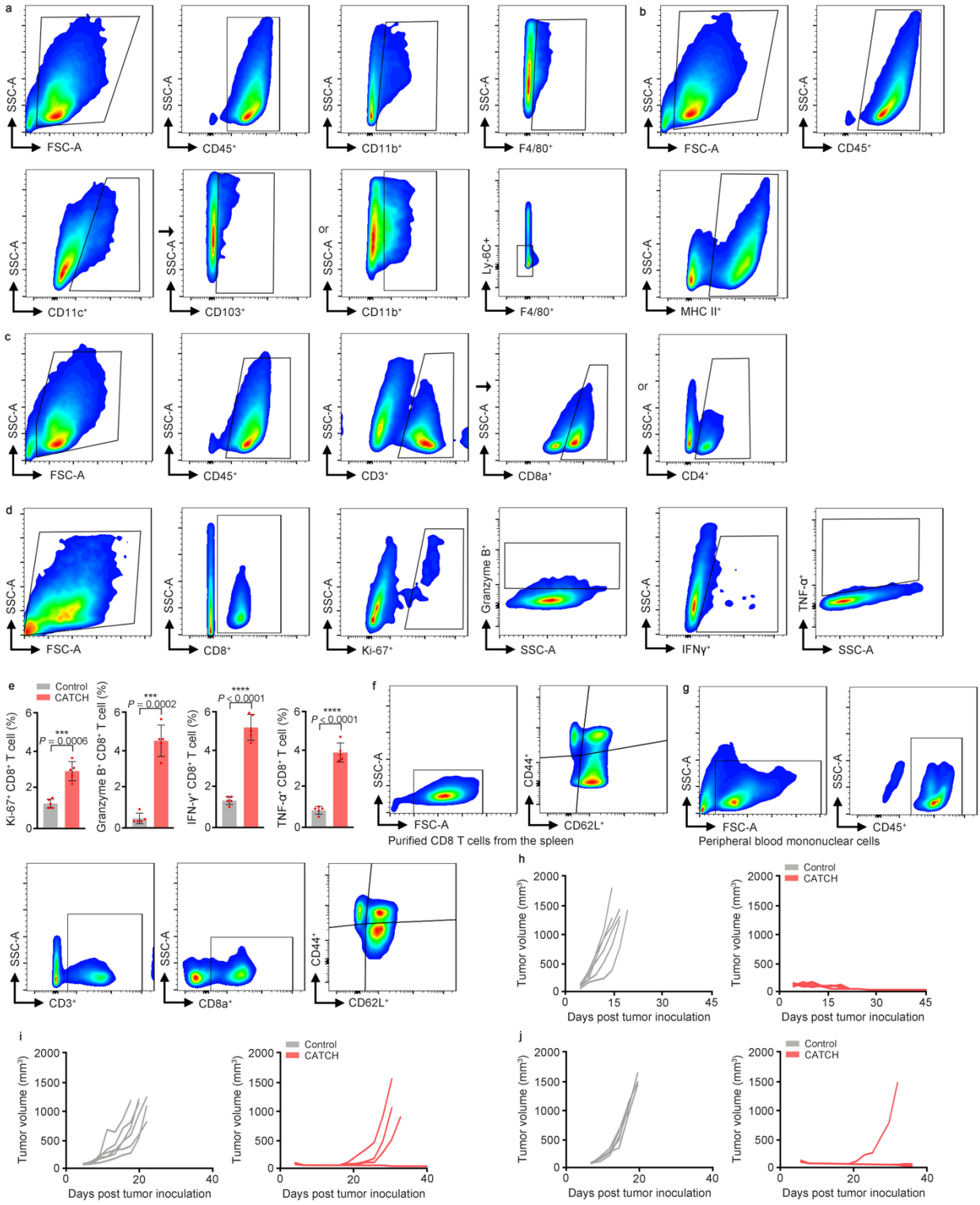
a
SSC-A
FSC-A
CD45+
CD11b+
F4/80+
b
MHC II+
CD11c+
CD103+
or
Ly-6C+
c
CD3+
CD8a+
CD4+
d
CD8+
Ki-67+
Granzyme B+
IFNγ+
TNF-α+
e
Control
CATCH
Ki-67+ CD8+ T cell (%)
Granzyme B+ CD8+ T cell (%)
IFN-γ+ CD8+ T cell (%)
TNF-α+ CD8+ T cell (%)
P = 0.0006
P = 0.0002
P < 0.0001
f
CD44+
CD62L+
Purified CD8 T cells from the spleen
g
Peripheral blood mononuclear cells
h
Tumor volume (mm3)
Days post tumor inoculation
i
j

Supplementary Fig. 9. Flow cytometry gating schemes of immune cells in tumor-draining lymph nodes and memory T cells, activation markers of *Pmel-1* $CD8^+$ T cells cocultured with DCs from tumoral tissues and tumor-draining lymph nodes, and tumor volume of individual mice. a, Flow cytometry gating schemes of macrophages. b, Flow cytometry gating schemes of conventional type 1 and type 2 dendritic cells (cDC1s and cDC2s). c, Flow cytometry gating scheme of $CD4^+$ and $CD8^+$ T cells. d, e, Flow cytometry gating schemes (d) and activation markers of *Pmel-1* $CD8^+$ T cells (e); n = 5 biologically independent mice. f, Flow cytometry gating schemes of memory T cells in the spleen. g, Flow cytometry gating schemes of memory T cells in the blood. h, Tumor volume of individual mice; n = 6. i, Tumor volumes over time; n = 6. j, Tumor volume of individual mice; n = 6. Data in e are presented as mean ± s.d. and statistical significance was analysed by two-tailed Student's *t*-test. $^{***}P < 0.001$, $^{****}P < 0.0001$.

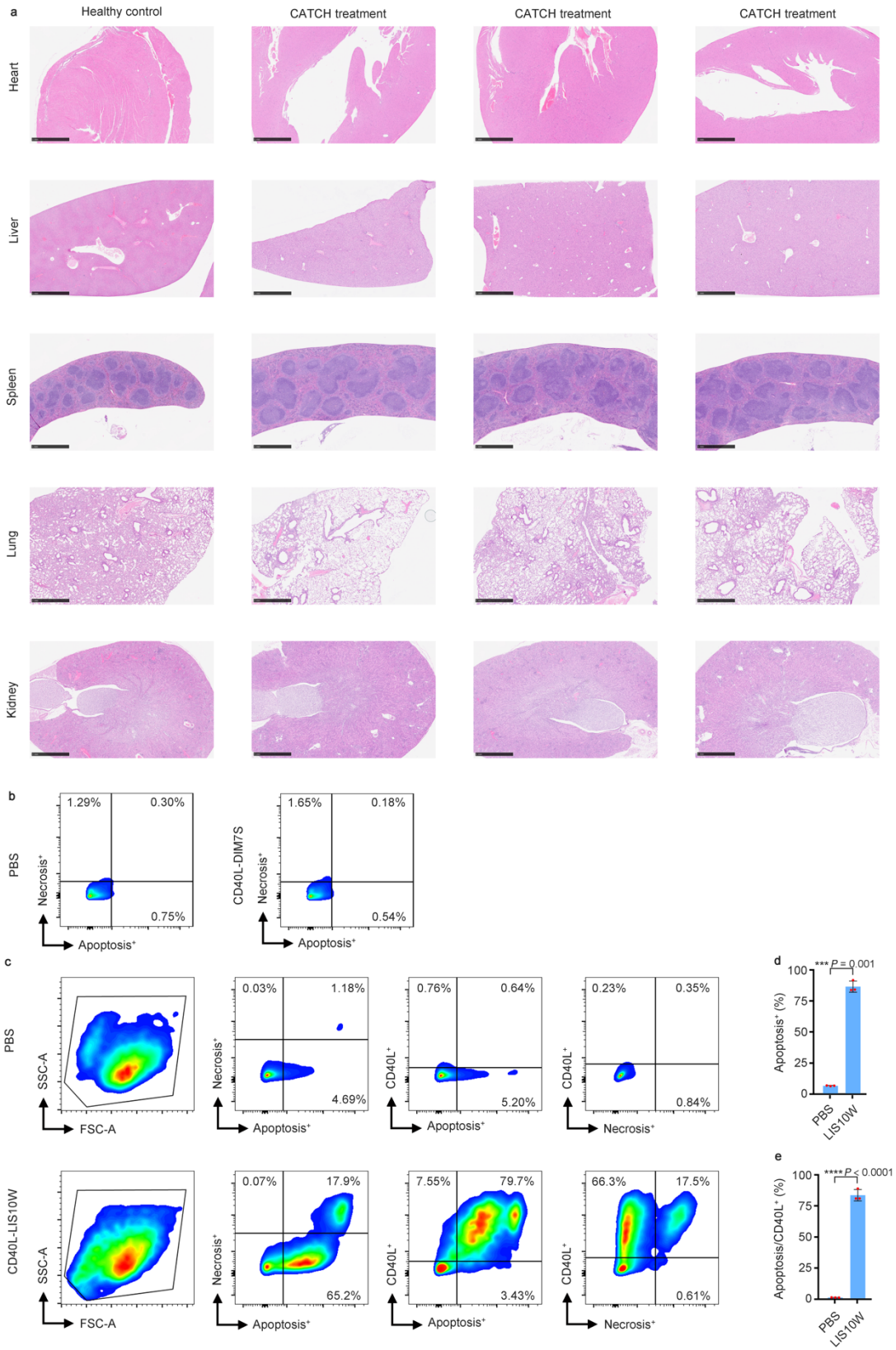
a
Healthy control
CATCH treatment
CATCH treatment
CATCH treatment
Heart
Liver
Spleen
Lung
Kidney
b
PBS
CD40L-DIM7S
1.29%
0.30%
0.75%
1.65%
0.18%
0.54%
Necrosis+
Apoptosis+
c
PBS
CD40L-LIS10W
SSC-A
FSC-A
0.03%
1.18%
4.69%
0.07%
17.9%
65.2%
0.76%
0.64%
5.20%
7.55%
79.7%
3.43%
0.23%
0.35%
0.84%
66.3%
17.5%
0.61%
CD40L+
d
*** P = 0.001
Apoptosis+ (%)
PBS
LIS10W
e
**** P < 0.0001
Apoptosis/CD40L+ (%)

Supplementary Fig. 10. Histopathology and CD40L expression and cytotoxicity induced by LIS10W in human cells. a, Histopathologic images from healthy mice and CATCH-treated mice, n = 3 biologically independent mice (scale bar = 1 mm). b, The cytotoxicity induced by DIM7S in human peripheral blood monocyte-derived dendritic cells (hPBDCs). c-e, Flow cytometry gating schemes (c), apoptosis (d), CD40L/apoptosis (e) mediated by CD40L-LIS10W in A375 human melanoma cells. Data in d and e are from n = 3 biologically independent samples and are presented as mean ± s.d. Statistical significance was analysed by two-tailed Student's *t*-test. ***$P < 0.001$, ****$P < 0.0001$.

References

1 Wculek, S. K. *et al*. Dendritic cells in cancer immunology and immunotherapy. *Nature Reviews Immunology* **20**, 7-24 (2020).

2 Chen, D. S. & Mellman, I. Oncology meets immunology: the cancer-immunity cycle. *Immunity* **39**, 1-10, doi:10.1016/j.immuni.2013.07.012 (2013).

3 Anguille, S., Smits, E. L., Lion, E., van Tendeloo, V. F. & Berneman, Z. N. Clinical use of dendritic cells for cancer therapy. *The lancet oncology* **15**, e257-e267 (2014).

4 Belderbos, R. A., Aerts, J. G. & Vroman, H. Enhancing dendritic cell therapy in solid tumors with immunomodulating conventional treatment. *Molecular Therapy-Oncolytics* **13**, 67-81 (2019).

5 Saxena, M., van der Burg, S. H., Melief, C. J. & Bhardwaj, N. Therapeutic cancer vaccines. *Nature Reviews Cancer* **21**, 360-378 (2021).

6 Spranger, S., Bao, R. & Gajewski, T. F. Melanoma-intrinsic β-catenin signalling prevents anti-tumour immunity. *Nature* **523**, 231-235 (2015).

7 Tang, M. *et al*. Toll-like receptor 2 activation promotes tumor dendritic cell dysfunction by regulating IL-6 and IL-10 receptor signaling. *Cell reports* **13**, 2851-2864 (2015).

8 Villablanca, E. J. *et al*. Tumor-mediated liver X receptor-α activation inhibits CC chemokine receptor-7 expression on dendritic cells and dampens antitumor responses. *Nature medicine* **16**, 98-105 (2010).

9 Veglia, F. *et al*. Lipid bodies containing oxidatively truncated lipids block antigen cross-presentation by dendritic cells in cancer. *Nature communications* **8**, 2122 (2017).

10 Gottfried, E. *et al*. Tumor-derived lactic acid modulates dendritic cell activation and antigen expression. *Blood* **107**, 2013-2021 (2006).

11 Harari, A., Graciotti, M., Bassani-Sternberg, M. & Kandalaft, L. E. Antitumour dendritic cell vaccination in a priming and boosting approach. *Nature Reviews Drug Discovery* **19**, 635-652, doi:10.1038/s41573-020-0074-8 (2020).

12 Kongsted, P. *et al*. Dendritic cell vaccination in combination with docetaxel for patients with metastatic castration-resistant prostate cancer: A randomized phase II study. *Cytotherapy* **19**, 500-513, doi:https://doi.org/10.1016/j.jcyt.2017.01.007 (2017).

13 Tanyi, J. L. *et al*. Personalized cancer vaccine effectively mobilizes antitumor T cell immunity in ovarian cancer. *Science translational medicine* **10**, eaao5931 (2018).

14 Saxena, M., Balan, S., Roudko, V. & Bhardwaj, N. Towards superior dendritic-cell vaccines for cancer therapy. *Nature biomedical engineering* **2**, 341-346 (2018).

15 Wojno, E. D. T., Hunter, C. A. & Stumhofer, J. S. The immunobiology of the interleukin-12 family: room for discovery. *Immunity* **50**, 851-870 (2019).

16 Böttcher, J. P. *et al*. NK Cells Stimulate Recruitment of cDC1 into the Tumor Microenvironment Promoting Cancer Immune Control. *Cell* **172**, 1022-1037.e1014, doi:https://doi.org/10.1016/j.cell.2018.01.004 (2018).
17 Fuertes, M. B. *et al*. Host type I IFN signals are required for antitumor CD8+ T cell responses through CD8{alpha}+ dendritic cells. *J Exp Med* **208**, 2005-2016, doi:10.1084/jem.20101159 (2011).
18 Mody, P. D. *et al*. Signaling through CD43 regulates CD4 T-cell trafficking. *Blood, The Journal of the American Society of Hematology* **110**, 2974-2982 (2007).
19 Baptista, A. P. *et al*. The chemoattractant receptor Ebi2 drives intranodal naive CD4+ T cell peripheralization to promote effective adaptive immunity. *Immunity* **50**, 1188-1201. e1186 (2019).
20 Chen, L. & Flies, D. B. Molecular mechanisms of T cell co-stimulation and co-inhibition. *Nature reviews immunology* **13**, 227-242 (2013).
21 Jhunjhunwala, S., Hammer, C. & Delamarre, L. Antigen presentation in cancer: insights into tumour immunogenicity and immune evasion. *Nature Reviews Cancer* **21**, 298-312 (2021).
22 Gaud, G., Lesourne, R. & Love, P. E. Regulatory mechanisms in T cell receptor signalling. *Nature Reviews Immunology* **18**, 485-497 (2018).
23 Yewdall, A. W., Drutman, S. B., Jinwala, F., Bahjat, K. S. & Bhardwaj, N. CD8+ T cell priming by dendritic cell vaccines requires antigen transfer to endogenous antigen presenting cells. *PloS one* **5**, e11144 (2010).
24 Jiang, Y., Li, Y. & Zhu, B. T-cell exhaustion in the tumor microenvironment. *Cell death & disease* **6**, e1792-e1792 (2015).
25 McLane, L. M., Abdel-Hakeem, M. S. & Wherry, E. J. CD8 T cell exhaustion during chronic viral infection and cancer. *Annual review of immunology* **37**, 457-495 (2019).
26 Seo, H. *et al*. BATF and IRF4 cooperate to counter exhaustion in tumor-infiltrating CAR T cells. *Nature immunology* **22**, 983-995 (2021).
27 Wagle, M. V. *et al*. Antigen-driven EGR2 expression is required for exhausted CD8+ T cell stability and maintenance. *Nature communications* **12**, 1-15 (2021).
28 Melero, I., Castanon, E., Alvarez, M., Champiat, S. & Marabelle, A. Intratumoural administration and tumour tissue targeting of cancer immunotherapies. *Nature Reviews Clinical Oncology* **18**, 558-576 (2021).
29 Knorr, D. A., Dahan, R. & Ravetch, J. V. Toxicity of an Fc-engineered anti-CD40 antibody is abrogated by intratumoral injection and results in durable antitumor immunity. *Proceedings of the National Academy of Sciences* **115**, 11048-11053 (2018).
30 Sandin, L. C. *et al*. Locally Delivered CD40 Agonist Antibody Accumulates in Secondary Lymphoid Organs and Eradicates Experimental Disseminated Bladder Cancer. *Cancer Immunology Research* **2**, 80-90, doi:10.1158/2326-6066.Cir-13-0067 (2014).
31 Irenaeus, S. M. *et al*. First-in-human study with intratumoral administration of a CD40 agonistic antibody, ADC-1013, in advanced solid malignancies. *International journal of cancer* **145**, 1189-1199 (2019).
32 Sheth, R. A. *et al*. Assessment of image-guided intratumoral delivery of immunotherapeutics in patients with cancer. *JAMA Network Open* **3**, e207911-e207911 (2020).

33 Sagiv-Barfi, I. *et al*. Therapeutic antitumor immunity by checkpoint blockade is enhanced by ibrutinib, an inhibitor of both BTK and ITK. *Proc Natl Acad Sci U S A* **112**, E966-972, doi:10.1073/pnas.1500712112 (2015).

34 Ouzounova, M. *et al*. Monocytic and granulocytic myeloid derived suppressor cells differentially regulate spatiotemporal tumour plasticity during metastatic cascade. *Nature communications* **8**, 14979 (2017).

35 Taggart, D. *et al*. Anti–PD-1/anti–CTLA-4 efficacy in melanoma brain metastases depends on extracranial disease and augmentation of CD8+ T cell trafficking. *Proceedings of the National Academy of Sciences* **115**, E1540-E1549 (2018).

36 Arvanitis, C. D., Ferraro, G. B. & Jain, R. K. The blood–brain barrier and blood–tumour barrier in brain tumours and metastases. *Nature Reviews Cancer* **20**, 26-41 (2020).

37 Datsi, A. & Sorg, R. V. Dendritic cell vaccination of glioblastoma: road to success or dead end. *Frontiers in Immunology*, 4506 (2021).

38 Jan, C.-I. *et al*. Predictors of response to autologous dendritic cell therapy in glioblastoma multiforme. *Frontiers in immunology* **9**, 727 (2018).

39 Pellegatta, S. *et al*. Intra-tumoral dendritic cells increase efficacy of peripheral vaccination by modulation of glioma microenvironment. *Neuro-Oncology* **12**, 377-388, doi:10.1093/neuonc/nop024 (2010).

40 Li, W. *et al*. Biomimetic nanoparticles deliver mRNAs encoding costimulatory receptors and enhance T cell mediated cancer immunotherapy. *Nature communications* **12**, 1-12 (2021).

41 Hewitt, S. L. *et al*. Durable anticancer immunity from intratumoral administration of IL-23, IL-36γ, and OX40L mRNAs. *Science translational medicine* **11**, eaat9143 (2019).

42 Hou, X. *et al*. Vitamin lipid nanoparticles enable adoptive macrophage transfer for the treatment of multidrug-resistant bacterial sepsis. *Nature nanotechnology* **15**, 41-46 (2020).

43 Sahay, G., Alakhova, D. Y. & Kabanov, A. V. Endocytosis of nanomedicines. *Journal of Controlled Release* **145**, 182-195, doi:https://doi.org/10.1016/j.jconrel.2010.01.036 (2010).

44 Geisler, J. A. *et al*. Modeling Brain Metastases Through Intracranial Injection and Magnetic Resonance Imaging. *JoVE (Journal of Visualized Experiments)*, e61272 (2020).

45 Zhang, Y. *et al*. STING agonist-derived LNP-mRNA vaccine enhances protective immunity against SARS-CoV-2. *Nano Letters* **23**, 2593-2600 (2023).

46 Zhang, X. *et al*. Functionalized lipid-like nanoparticles for in vivo mRNA delivery and base editing. *Science advances* **6**, eabc2315 (2020).

47 Hong, J., Radojcic, D., Ionescu, M., Petrovic, Z. S., Eastwood, E. Advanced Materials from Corn: Isosorbide-Based Epoxy Resins. *Polym. Chem.* **5**, 5360-5368 (2014).

48 Wroblewska, A., Zych, A., Thiyagarajan, S., Dudenko, D., van Es, D., Hansen, M. R., Koning, C., Duchateau, R., Jasinska-Walc, L. Towards Sugar-Derived Polyamides as Environmentally Friendly Materials. *Polym. Chem.* **6**, 4133-4143 (2015).